Dual targeting of PDPK1 and BRAF V600E is synthetically lethal

Tejinder Pal Khaket[1*], Chandrayee Ghosh[1], Zhongyue Yang[1], Myriem Boufraqech[3], Jiangnan Hu[1], Eden D. Alamaw[4], Thorkell Andresson[6], Maura O'Neill[6], Ya-Qin Zhang[7], Min Shen[7], Bereketeab Haileselassie[8], Electron Kebebew[1,2**]

[1]Department of Surgery, Stanford University, Stanford, CA, USA

[2]Stanford Cancer Institute, Stanford University, Stanford, CA, USA

[3]Surgical Oncology Branch, Center for Cancer Research, National Cancer Institute, NIH, MD, USA

[4]Department of Comparative Medicine, Stanford University, CA, USA

[5]Department of Comparative Medicine, Veterinary Service Center, Stanford University, Stanford, CA, USA.

[6]Protein and Metabolite Characterization Core, Cancer Research Technology Program, Frederick National Laboratory for Cancer Research, Frederick, MD, USA

[7]National Center for Advancing Translational Sciences, National Institute of Health, Bethesda, MD, USA

[8]Lucile Packard Children's Hospital, Stanford University, CA, United States

Corresponding Authors:

*Tejinder Pal Khaket, tpkhaket@stanford.edu

** Electron Kebebew, kebebew@stanford.edu

28 **ABSTRACT**

29 **Purpose:** PDPK1 functions downstream of PI3K and is essential for activating AKT and other
30 AGC kinases. Although PDPK1 has a central role in the PI3K/AKT/mTOR signaling pathway,
31 there has been limited evaluation of it as a target for cancer therapy. Anaplastic thyroid cancer
32 (ATC) has one of the highest mortality rates of all human malignancies. Although combined BRAF
33 and MEK inhibition in *BRAF* V600E–mutant ATC (45% of cases) results in response, resistance
34 is common, and there is no curative treatment. The majority (up to 95.8%) of ATC cases have
35 activation in the PI3K/AKT/mTOR and RAS/RAF/MEK/MAPK pathways due to genetic
36 alterations (including driver mutations and genomic gains/losses), involved in these pathways. In
37 this study, we investigated PDPK1 as a therapeutic target for ATC.

38 **Experimental design:** We used *in vitro*, *ex vivo*, and *in vivo* ATC models to evaluate the effect of
39 targeting PDPK1 (BX795) alone and in combination with mutated *BRAF* V600E inhibition
40 (dabrafenib), and the mechanism of action that resulted in ATC cell death.

41 **Results:** BX795 monotherapy significantly reduced ATC cell proliferation, invasion, colony
42 formation, and spheroid size. The combination of BX795 with dabrafenib produced strong
43 synergistic antitumor activity in *BRAF* V600E-mutant ATC models. Dual inhibition led to
44 simultaneous and sustained suppression of PDPK1/AKT and MAPK signaling, preventing the
45 compensatory pathway reactivation observed with single-agent treatment. This integrated
46 blockade induced pronounced oxidative stress, DNA damage, and G2-phase cell-cycle arrest,
47 accompanied by mitochondrial dysfunction and robust activation of apoptotic cascades. These
48 effects translated into marked tumor regression in in vitro, ex vivo, and in vivo experimental
49 systems.

50 **Conclusions:** Our findings identify PDPK1 as a critical and therapeutically tractable vulnerability
51 in anaplastic thyroid cancer. Co-targeting PDPK1 and *BRAF* V600E produces potent synergistic

antitumor activity by shutting down convergent oncogenic signaling nodes and amplifying apoptotic stress responses. These data support PDPK1 inhibition—alone and in combination with BRAF blockade acts as a promising strategy to improve outcomes for patients with *BRAF* V600E-mutant ATC.

Keywords: Anaplastic thyroid cancer; PDPK1, *BRAF* V600E mutation, BX795, cell cycle arrest, synergism

59 **INTRODUCTION**

60 Anaplastic thyroid cancer (ATC) is a rare (incidence of 1–2 cases per million people) and
61 lethal cancer. Although ATC accounts for 1%–2% of all thyroid cancer cases, it is responsible for
62 two-thirds of all thyroid cancer deaths and has a median survival time of only 6 months (1–3).
63 Recent advances in the understanding of genetic alterations in ATC have revealed that the majority
64 (up to 95.8%) of ATC cases have activation in the PI3K/AKT/mTOR and MAPK/ERK (also
65 known as RAS/RAF/MEK/MAPK) pathways due to genomic alterations (driver mutations and
66 genomic gains/losses) involved in these pathways (4,5). Targeting driver mutations, such as *BRAF*
67 V600E (present in 45% of ATC cases), in mutant ATC elicits a response in some cases, but
68 development of resistance to treatment and treatment-related toxicity that results in treatment
69 stoppage are common (3,6–10). Thus, there is an urgent need to develop new therapeutic strategies
70 for ATC that elicit a significant and durable response and thereby extend patient survival.

71 Although inhibition of the MAPK/ERK pathway in *BRAF* V600E–mutant ATC, using
72 BRAF and MEK inhibitors, is effective, compensatory upregulation and acquired mutations in the
73 PI3K/AKT/mTOR pathway commonly undermine this strategy, leading to therapeutic resistance
74 (11–16). Within the PI3K/AKT/mTOR signaling pathway, 3-phosphoinositide-dependent kinase 1
75 (PDPK1 or PDK1) functions downstream of PI3K and is essential for activating AKT and other
76 AGC kinases (17,18). Although PDPK1 has a central role in the PI3K/AKT/mTOR signaling
77 pathway, there has been limited investigation of it as a target for cancer therapy (18). Gene
78 mutations that lead to activation of the PI3K/AKT/mTOR pathway are common in ATC and occur
79 in genes upstream of PDPK1. However, direct evidence of PDPK1 phosphorylation in ATC has
80 not yet been reported, representing an important knowledge gap. Phosphorylation of PDPK1 at
81 Ser241 is essential for its activity in phosphorylating AKT at Thr308 and its association with
82 cancer initiation and progression (19). PDPK1 overexpression drives cancer initiation and

83 progression in a range of malignancies, and is associated with more aggressive tumors (20–38).
84 PDPK1 is also overexpressed in thyroid cancer, where higher levels are associated with more
85 advanced disease and ATC (39). Accumulating evidence indicates that PDPK1-mediated AKT
86 activation plays a central role in cancer initiation and progression (40–44).

87 Investigating PDPK1 activation in ATC could provide both mechanistic insight and define
88 the potential of targeting it for ATC therapy and other cancers with activation in the
89 PI3K/AKT/mTOR pathway. Therefore, we evaluated the anticancer activity of targeting PDPK1
90 using *in vitro*, *ex vivo*, and *in vivo* models in ATC with and without *BRAF* V600E inhibition.

91

92 **MATERIALS AND METHODS**

93 **Materials**

94 The materials used in this study are listed in Tables S1 (list of antibodies), S2 (list of
95 chemicals), and S3 (cell lines and their mutation status).

96

97 **Cell lines and culture conditions**

98 The homozygous mutated *BRAF* V600E 8505C, FTC133 (homozygous mutated *PTEN*),
99 and FTC236 (homozygous mutated *PTEN*) human thyroid cancer cell lines were purchased from
100 the European Collection of Cell Culture (Salisbury, UK). The heterozygous mutated *BRAF* V600E
101 human ATC cell line SW1736 and the *BRAF* wild type ATC cell line C643 (heterozygous mutated
102 *PTEN*) were purchased from Cell Lines Service GmbH (Eppelheim, Germany). The THJ-11T
103 (*KRAS* mutant), THJ-29T, and THJ-16T (*PIK3CA* mutant) ATC cell lines were a kind gift from Dr.
104 John A. Copland III (Mayo Clinic, Jacksonville, FL). The BCPAP (homozygous mutated *BRAF*
105 V600E) cell line was purchased from Leibniz Institute DSMZ (Lower Saxony, Germany). The
106 TPC1 (*RET/PTC1* rearrangement) cell line was purchased from Sigma-Aldrich, Inc. (St. Louis,

107 MO, USA). Details of cell line–specific mutations are provided in Table S3. The HEK293 cell line
108 was purchased from American Type Culture Collection (Manassas, VA, USA). All cells were
109 cultured in Dulbecco's Modified Eagle's Medium (DMEM, which contains 4,500 mg/L of D-
110 glucose, 2 mmol/L of L-glutamine, and 110 mg/L of sodium pyruvate) supplemented with 10%
111 fetal bovine serum (FBS), and antibiotics (penicillin and streptomycin at 10,000 U/mL) at 37 °C
112 and 5% CO_2. Two patient-derived *BRAF* V600E–mutant ATC cell lines—ATC-01, derived from a
113 treatment-naïve patient's primary *BRAF* V600E–mutant tumor, and ATC-02, derived from a *BRAF*
114 V600E–mutant residual tumor following combination therapy with dabrafenib (Dab) and
115 trametinib (*BRAF* and MEK inhibitors, respectively)—were maintained in DMEM:F12
116 supplemented with 15% FBS and antibiotics (penicillin and streptomycin at 10,000 U/mL) at 37
117 °C and 5% CO_2 in a humidified incubator.
118
119 **Quantitative high-throughput screening**
120 Quantitative high-throughput screening was used to screen the 8505C, THJ-11T, and THJ-
121 16T ATC cell lines based on the National Center for Advancing Translational Sciences (NCATS)
122 Pharmaceutical Collection (NPC) and the Mechanism Interrogation PlatE (MIPE) library with
123 4,991 small-molecule drugs and investigational compounds. Cell viability was measured using a
124 luciferase-coupled adenosine triphosphate (ATP) quantitation assay (CellTiter-Glo®, Promega,
125 Madison, WI, USA). To identify the optimal PDPK1 inhibitor, drug response data of PDPK1
126 inhibitors (BX-912, DTXSID90678515, OSU-03012, GSK-2334470, and BX795) present in the
127 high-throughput screening library were analyzed.
128
129 **Cell proliferation assay**

130 Cells were seeded in 96-well black plates (Greiner Bio-One, Kremsmünster, Austria) at a
131 density of 1.5×10^3 cells per well. After 24 h, cells were treated in triplicate with the indicated
132 concentrations of Dab, BX795, and other small molecules for 48 h at 37 °C and 5% CO_2 in a
133 humidified incubator. Dimethyl sulfoxide (DMSO) was used as a vehicle control. CyQUANT cell
134 proliferation assays were performed according to the manufacturer's instructions, and the results
135 were analyzed using a SpectraMax i3x Multi-Mode Microplate Reader (Molecular Devices, San
136 Jose, CA, USA) at an excitation wavelength of 480 nm and an emission wavelength of 530 nm.
137 The relative fold change was measured as compared to the control. Statistical analyses were
138 performed using GraphPad Prism version 10 (GraphPad Software Inc., San Diego, CA, USA).
139

140 **Calculation of combination drug activity**

141 After treating ATC cells with various concentrations of DMSO (control), BX795, Dab, or
142 their combination (BX795 + Dab) for 48 h, cell proliferation was measured. Then, drug responses
143 were analyzed using the CompuSyn software (Version 1.0) based on the Chou–Talalay method
144 (45) to determine synergy, additivity, or antagonism. The combination index (CI) was calculated,
145 where CI < 1 indicates synergy, CI = 1 indicates an additive effect, and CI > 1 indicates
146 antagonism. The values were derived from drug combinations applied at non-constant ratios.
147

148 **Clonogenic assay**

149 Cells (1×10^3 cells/well) were seeded in 12-well plates and allowed to adhere overnight.
150 Then, cells were treated in triplicate with DMSO (control), BX795 (2.5 μM), Dab (2.5 μM), or
151 their combination (BX795 + Dab) for 48 h, after which time the medium was replaced with fresh
152 complete DMEM, and colonies were allowed to form for up to 8–12 days. Colonies were fixed
153 with 4% buffered paraformaldehyde for 10 min at room temperature, washed with phosphate-

154 buffered saline (PBS), and then stained with 0.5% crystal violet for 30 min at room temperature
155 with continuous shaking. Finally, stained colonies were washed with water, and the ImageJ
156 software (National Institutes of Health, Bethesda, MD, USA) was used for quantification.
157 GraphPad Prism version 10 was used for statistical analysis.
158
159 **Migration assay**
160 A wound-healing assay was performed to analyze cellular migration. In brief, a scratch
161 (wound) was generated using a sterile pipette tip, and cells were washed with PBS; treated in
162 triplicate with DMSO (control), BX795 (2.5 μM), Dab (2.5 μM), or their combination (BX795 +
163 Dab); and incubated in DMEM supplemented with 2% FBS for 16–24 h. Finally, wound-healing
164 was measured using ImageJ. The results are presented as the relative change in cellular migration
165 compared to the control.
166
167 **Spheroid formation assay**
168 Mutant *BRAF* V600E ATC cells (8505C, SW1736, ATC01, and ATC02) were seeded in
169 round bottom, ultra-low attachment 96-well plates (1.5×10^3/well) using 3D Tumorsphere Medium
170 XF (PromoCell, Heidelberg, Germany) and placed in a humidified incubator at 37 °C with 5%
171 CO_2 for spheroid formation. After 72 h, spheroids were treated with DMSO (control), BX795 (2.5
172 μM), Dab (2.5 μM), or their combination (BX795 + Dab), and monitored over 7 days. Images of
173 each spheroid were acquired after 0 and 8 days of treatment. The size was quantified using ImageJ.
174 The data are presented as the relative change in spheroid size compared to the control.
175
176 **Quantitative proteomic and phosphoproteomic analysis**
177 ***Sample preparation and tandem mass tag (TMT) labeling***

178 Mutant BRAF V600E ATC cell lines were treated with DMSO (control), BX795 (2.5 μM),
179 Dab (2.5 μM), or their combination (BX795 + Dab) for 48 h. Cell pellets were resuspended in 200
180 μL of EasyPep™ lysis buffer (Thermo Fisher Scientific, Waltham, MA, USA) supplemented with
181 nuclease (1 μL), protease inhibitors, and PhosSTOP (Sigma-Aldrich, Inc., St. Louis, MO, USA).
182 Protein concentrations were determined with the BCA protein assay, and 100 μg of protein per
183 sample was mixed with 50 μL of reduction reagent and 50 μL of alkylation reagent. Samples were
184 digested overnight at 37 °C with 6 μg of trypsin/Lys-C at 750 rpm. The following day, 200 μg of
185 the TMTpro reagent (Thermo Scientific) was added, and samples were incubated for 1 h at 25 °C.
186 Labeling reactions were quenched with 5% hydroxylamine and 20% formic acid (50 μL, 10 min).
187 TMT-labeled peptides were combined, cleaned using the EasyPep™ Maxi Kit, and dried in a
188 vacuum concentrator.
189
190 ***Phosphopeptide enrichment***
191 Sequential phosphopeptide enrichment was performed using the High-Select TiO_2 and Fe-
192 NTA IMAC kits (Thermo Fisher Scientific) following the manufacturer's protocols. Peptides were
193 first enriched by TiO_2; the TiO_2 flow-through and wash fractions were collected, dried, and
194 subjected to a second enrichment using immobilize metal affinity chromatography (IMAC). Eluted
195 phosphopeptides from both steps were combined, dried, and reserved for liquid chromatography–
196 tandem mass spectrometry (LC–MS/MS) analysis. IMAC flow-through and wash fractions were
197 saved for high-pH fractionation.
198
199 ***High-pH reverse-phase fractionation***
200 IMAC flow-through peptides were resuspended in 100 μL of LC/MS-grade water, and 85
201 μL was fractionated by high-pH reverse-phase ultra-performance liquid chromatography (UPLC)

202 (ACQUITY, Waters, Milford, MA). Peptides were separated on a 150 mm × 3.0 mm XBridge
203 Peptide BEH C18 column (2.5 µm) at 0.35 mL/min. After a 5-min wash with mobile phase A (10
204 mM ammonium formate, pH 9.4), peptides were eluted using a gradient of 10%–50% mobile phase
205 B (10 mM ammonium formate/90% acetonitrile, pH 9.6; 5–60 min), followed by 50%–75% B
206 (60–70 min). Fractions were collected every minute, generating 60 fractions, which were pooled
207 into 12 final fractions, dried, and stored at −80 °C until analysis.
208
209 ***LC–MS/MS analysis***
210 Dried fractions were resuspended in 0.1% formic acid, and 5 µL was injected into a Dionex
211 UltiMate 3000 RSLC system coupled to an Orbitrap Eclipse mass spectrometer (Thermo Fisher
212 Scientific) equipped with FAIMS and an EasySpray source. Chromatographic separation was
213 performed at 300 µL/min using solvent A (0.1% formic acid) and solvent B (80% acetonitrile/0.1%
214 formic acid) with the following gradient: 5%–7% B (1 min), 7%–30% B (83 min), 30–59% B (25
215 min), 50%–95% B (4 min), 95% B (7 min), and re-equilibration at 5% B (17 min). The mass
216 spectrometer was operated in TopSpeed mode using four FAIMS compensation voltages (−45,
217 −55, −65, and −75). MS1 scans were acquired in the Orbitrap at 120,000 resolutions with an
218 automatic gain control (AGC) target of 4×10^5 and a maximum injection time of 50 ms over 375–
219 1600 m/z. MS2 spectra were acquired using the TurboTMT method at 15,000 resolutions (an AGC
220 target of 5×10^4, an isolation window of 1.6 m/z, a higher-energy collisional dissociation [HCD]
221 of 30%, and a minimum intensity of 2.5×10^4). Monoisotopic precursor selection, Easy-IC internal
222 calibration, and advanced peak determination were enabled. For phosphopeptide runs, two FAIMS
223 methods were used, each containing four compensation voltages (CVs) (a cycle time of 0.75 s per
224 CV; 3 s total): Method 1 (−45, −55, −65, and −75) and Method 2 (−50, −60, −70, and −80).
225

226 ***Database searching and quantification***

227 Raw files were processed in Proteome Discoverer using the Sequest HT node. Spectra were
228 searched against the UniProt human database with full trypsin specificity, allowing up to two
229 missed cleavages and a minimum peptide length of six residues. Tolerance was set to 10 ppm for
230 MS1 and 0.02 Da for MS2. Carbamidomethylation of cysteine, TMTpro labeling of lysine and
231 peptide N-termini, and phosphorylation of serine/threonine/tyrosine were specified as static or
232 variable modifications as appropriate. Methionine oxidation was included as a variable
233 modification. PSM-, peptide-, and protein-level false-discovery rates (FDRs) were controlled with
234 Percolator. Reporter ion intensities were quantified using the Reporter Ion Quantifier node and
235 normalized to the total peptide abundance per channel.

236

237 ***Proteomic and phosphoproteomic data analysis and pathway enrichment***

238 All proteomic and phosphoproteomic analyses were performed in R version 4.2 using a
239 reproducible workflow. The data were imported with readr (v2.1.4) and processed using dplyr
240 (v1.1.4) and tidyr (v1.3.0), with removal of contaminants and low-confidence entries. Phosphosite-
241 level specificity was preserved by generating unique feature identifiers combining gene symbol
242 and phosphorylation site annotation (*Gene|site_label*), and numeric columns were explicitly
243 coerced to the numeric format. Differential abundance or phosphorylation was assessed for each
244 treatment condition (BX795, Dab, and their combination) relative to the control, yielding $\log_2$ fold
245 changes ($\log_2$FCs) and associated p-values, with multiple testing correction applied using the
246 Benjamini–Hochberg method. Volcano plots ($\log_2$FC versus $-\log_{10}$(p-value)) and Venn diagrams
247 of significantly regulated features were generated using ggplot2 (v3.4.4), ggrepel (v0.9.4), and
248 ggVennDiagram (v1.2.2). Gene set enrichment analysis (GSEA) was performed with fgsea
249 (v1.28.0) using a signed ranking metric (sign($\log_2$FC) × $-\log_{10}$(p-value)) and curated Kyoto

250 Encyclopedia of Genes and Genomes (KEGG) and MSigDB Hallmark gene sets, reporting
251 normalized enrichment scores (NESs) with FDR-adjusted q-values. In addition, enrichment
252 heatmaps were produced with pheatmap (v1.0.12). All figures were exported at publication-quality
253 resolution.
254
255 **Cell cycle analysis**
256 Mutant *BRAF* V600E ATC cells (8505C and SW1736) were treated overnight with DMSO
257 (control), BX795 (2.5 μM), Dab (2.5 μM), or their combination (BX795 + Dab). Then, cells were
258 trypsinized and fixed using pre-chilled 70% ethanol, followed by overnight incubation at –80 °C.
259 The next day, cells were thawed and centrifuged at 1500 rpm for 5 min, washed with PBS, and
260 stained with FxCycle™ PI/RNase staining solution (Thermo Fisher Scientific) for 30 min at room
261 temperature. After incubation, the cell cycle and DNA content (2N or 4N) were analyzed with a
262 BD Accuri C6 Plus flow cytometer (BD Biosciences, San Jose, CA, USA). Experiments were
263 performed in triplicate, and the results are reported compared to the control.
264
265 **Apoptosis assay**
266 Apoptotic cells were identified using the Annexin V/Dead Cell Apoptosis Kit (BD
267 Biosciences) as per the manufacturer's protocol. Briefly, mutated *BRAF* V600E ATC cells (8505C
268 and SW1736) were treated for 48 h with DMSO (control), BX795 (2.5 μM), Dab (2.5 μM), or
269 their combination (BX795 + Dab). Then, cells were harvested, trypsinized, and washed with ice-
270 cold PBS. The single-cell suspension was resuspended in 100 μL of 1× annexin-binding buffer
271 with 5 μL each of Annexin V and propidium iodide (PI), followed by incubation for 20 min at
272 room temperature. Annexin V/PI-stained cells were measured using a BD Accuri C6 Plus flow
273 cytometer (BD Biosciences). The relative fold change was determined compared to the control.

274

275 **Reactive oxygen species (ROS) measurement**

276 Cellular ROS were measured using DCHFDA staining. Mutant *BRAF* V600E ATC cells
277 (8505C and SW1736) were treated 24h with DMSO (control), BX795 (2.5 μM), Dab (2.5 μM), or
278 their combination (BX795 + Dab). After treatment, cells were trypsinized, washed with PBS, and
279 stained with DCHFDA (5 μM) for 30 min in the dark. After incubation, DCHFD fluorescence was
280 measured using a BD Accuri C6 Plus flow cytometer (BD Biosciences). The results are presented
281 as relative fold change compared to the control.

282 Mitochondrial ROS production was measured using Mito-SOX™ Red mitochondrial
283 superoxide indicator. After treatment overnight, cells were harvested, trypsinized, washed with
284 PBS, and stained with 2.5 μM Mito-SOX Red for 20 min at 37 °C. Mito-SOX™ fluorescence was
285 measured using a BD Accuri C6 Plus flow cytometer (BD Biosciences). The results are presented
286 as relative fold change compared to the control.

287

288 **Mitochondrial content measurement**

289 Mitochondria were visualized using MitoTracker Green FM (Thermo Fisher Scientific),
290 which labels mitochondria independently of the membrane potential. Mutant *BRAF* V600E ATC
291 cells (8505C and SW1736) were seeded onto sterile coverslips in 12-well plates; allowed to adhere
292 overnight; and treated with DMSO (control), BX795 (2.5 μM), Dab (2.5 μM), or their combination
293 (BX795 + Dab). After treatment, cells were stained with 50 nM MitoTracker Green for 30 min at
294 37 °C in the dark. Then, cells were washed with PBS, and live cell fluorescence imaging was
295 acquired using a SP8 confocal microscope (Leica, Wetzlar, Germany) at 400× magnification under
296 identical acquisition settings for all samples at multiple sites on each slide. Fluorescence intensity
297 was quantified using ImageJ.

298 In addition, single-cell suspensions of treated cells were stained in triplicate with 50 nM
299 MitoTracker Green FM for 30 min at 37 °C in the dark. Cellular fluorescence was measured using
300 a BD Accuri C6 Plus flow cytometer (BD Biosciences). The results are presented as the relative
301 fold change compared to the control.
302
303 **Measurement of mitochondrial transmembrane potential**
304 The mitochondrial membrane potential was analyzed by using the Image-iT™ TMRM
305 Reagent (Thermo Fisher Scientific). Mutant *BRAF* V600E ATC cells (8505C and SW1736) were
306 treated overnight in triplicate with DMSO (control), BX795 (2.5 μM), Dab (2.5 μM), or their
307 combination (BX795 + Dab). After treatment, cells were trypsinized, and single-cell suspensions
308 were stained with TMRM (100 nM) for 30 min at 37 °C in the dark. Following treatment, cells
309 were washed and resuspended in ice-cold PBS. Fluorescence was measured using a BD Accuri C6
310 Plus flow cytometer (BD Biosciences). The results are presented as the relative fold change
311 compared to the control.
312 Mitochondrial depolarization was measured with the potentiometric dye JC-1. After
313 treatment 24h with DMSO (control), BX795 (2.5 μM), Dab (2.5 μM), or their combination
314 (BX795 + Dab), mutant *BRAF* V600E ATC cells (8505C and SW1736) were stained with JC-1
315 (2 μM) for 30 min at 37 °C in the dark, washed, and resuspended in ice-cold PBS. Red and green
316 fluorescence was measured using a BD Accuri C6 plus flow cytometer (BD Biosciences). The
317 results are presented as the relative ratio of red versus green fluorescence compared to the control.
318
319 **Measurement of the oxygen consumption rate (OCR)**
320 The OCR was measured using a Seahorse XFe24 Extracellular Flux Analyzer (Seahorse
321 Bioscience, Santa Clara, CA). Mutant *BRAF* V600E ATC cells (8505C and SW1736) were seeded

322 evenly in XF24 microplates; allowed to adhere for 24 h; and then treated for an additional 24 h
323 with DMSO (control), BX795 (2.5 μM), Dab (2.5 μM), or their combination (BX795 + Dab).
324 Measurements were performed in XF assay medium containing 1 mM sodium pyruvate, 2 mM
325 glutamine, and 10 mM glucose under basal conditions. After washing with assay medium, cells
326 were incubated at 37 °C in a non-CO_2 incubator for 30 min. The baseline OCR was recorded,
327 followed by sequential injections of oligomycin (1 μM, an ATP synthase inhibitor), FCCP (4 μM,
328 a mitochondrial uncoupler), rotenone (1 μM, a complex I inhibitor), and antimycin A (1 μM, a
329 complex III inhibitor) using Seahorse XFe24 Extracellular Flux Analyzer (Seahorse Bioscience).
330 Mitochondrial function parameters were calculated as follows: basal OCR = baseline OCR − OCR
331 after rotenone/antimycin A; ATP-linked OCR = basal OCR − OCR after oligomycin; maximal
332 respiration = OCR after FCCP − OCR after rotenone/antimycin A. The assay involved 3 min of
333 mixing, 3 min of waiting, and 3 min of measurement. The data were normalized to the total protein
334 content and are presented as the mean ± standard deviation (SD).
335
336 **Western blot analysis**
337 Lysates from mutant *BRAF* V600E ATC cells (8505C and SW1736) were prepared in
338 radioimmunoprecipitation assay (RIPA) buffer supplemented with phosphatase and protease
339 inhibitors. Protein concentrations were determined using the Pierce™ BCA Protein Assay Kit
340 (Thermo Fisher Scientific). Equal amounts of protein were separated by electrophoresis on 4%–
341 15% precast sodium dodecyl sulfate–polyacrylamide gel electrophoresis (SDS-PAGE) gels and
342 transferred to nitrocellulose membranes. Membranes were incubated overnight at 4 °C with
343 primary antibodies (Table S1), followed by horseradish peroxidase (HRP)-conjugated secondary
344 antibodies (Table S1). Protein bands were visualized using enhanced chemiluminescence (ECL)

345 and imaged with a Bio-Rad ChemiDoc™ MP Imaging System (Bio-Rad, Hercules, CA, USA).
346 Band intensities were quantified using ImageJ.
347
348 **Immunofluorescence**
349 Mutant *BRAF* V600E ATC cells (8505C and SW1736) were treated overnight with DMSO
350 (control), BX795 (2.5 μM), Dab (2.5 μM), or their combination (BX795 + Dab). Then, cells were
351 washed with PBS, fixed 3 × 15 min using chilled methanol, washed 3 × 5 min with PBS,
352 permeabilized by PBS containing 0.2%Triton X-100, and finally washed three times with PBS.
353 Cells were incubated with 1% bovine serum albumin containing 0.02% Tween 20 for 30 min at
354 room temperature (to block nonspecific protein binding), followed by incubation overnight with
355 the pH_2AX primary antibody (Table S1) at 4 °C. The next day, cells were washed three times with
356 PBS containing 0.02% Tween 20 (PBST) and incubated with fluorescently labelled secondary
357 antibodies (Table S1) for 2 h at room temperature. Finally, cells were washed with PBST and
358 counterstained with mounting media containing DAPI. Labelled proteins were observed using an
359 SP8 confocal microscope (Leica) at 400× magnification. The number of H2AX foci among 25
360 cells was counted for each treatment. The results are presented as the number of foci (mean ±
361 standard error of the mean [SEM]).
362
363 **Orthotopic ATC xenograft model**
364 For the orthotopic ATC model, 1×10^6 8505C-Luc2 cells (Luc2 denotes cells with stable
365 expression of a luciferase reporter) were implanted into the thyroid gland of male and female *NOD*
366 *Cg-Prkdcs^{cid} Il2rg^{tm1Wjl}/SzJ* mice. All animal procedures were approved by the Stanford
367 Administrative Panel on Laboratory Animal Care (APLAC; Protocol #34767) and conducted in
368 accordance with institutional and federal guidelines. Tumor luminescence was measured using the

369 Lago (Spectral Instruments Imaging, Tucson, AZ, USA) after intraperitoneal luciferin injection
370 (150 mg/kg). One week after orthotopic implantation, 10 mice (5 males and 5 females) were
371 randomized into four treatment groups: vehicle control (CM-cellulose), BX795 (100 mg/kg), Dab
372 (15 mg/kg), and BX795 (100 mg/kg) + Dab (15 mg/kg). BX795 and Dab were solubilized in
373 methyl cellulose (0.5% in double-distilled water) with sonication (Picoruptor, Diagenode Inc,
374 Devville, NJ, USA) at 4 °C. They were administered orally 5 days/week for 2 weeks with
375 continuous monitoring for toxicity. Mice were imaged and weighed weekly. After treatment, all
376 mice were euthanized using CO_2 inhalation. Tumor, lung, and liver samples were collected after
377 euthanasia. Tumor size and weight were recorded, and thyroid tumor, lung, liver, and kidney
378 samples were collected for histopathological evaluation.
379
380 **Statistical analyses**
381 The data are presented as the mean ± SD, with the details for each analysis provided in the
382 figure legends. Note that the *in vivo* results and number of H_2AX foci are presented as the mean ±
383 SEM. All *in vitro* experiments were performed in at least three independent experiments. Analysis
384 of variance (ANOVA) was used to determine the differences between groups. GraphPad Prism
385 version 10 (GraphPad Software, San Diego, CA) was used for all statistical analyses. The level of
386 statistical significance is indicated as follows: ns is nonsignificant; *$p < 0.05$; **$p < 0.01$; ***$p <$
387 0.001; and ****$p < 0.0001$.
388
389 **RESULTS**
390 **Functional dependency on PDPK1 in ATC**
391 To assess PDPK1 as a therapeutic vulnerability in ATC, we integrated DepMap CRISPR
392 Chronos dependency scores with PDPK1 expression across cancer lineages. PDPK1 showed broad

393 essentiality (median Chronos ≈ –0.88), with thyroid cancers clustering among the highly
394 dependent groups, comparable to bowel and pancreatic cancers. Within the thyroid lineage,
395 PDPK1 transcript levels were similar across medullary, well-differentiated, and anaplastic thyroid
396 cancer cell lines (Fig. S1A–B). In contrast, functional dependency analysis revealed marked
397 PDPK1 dependence in both ATC (Chronos –0.65 to –1.15; median –0.84) and WDTC (–0.606 to
398 –1.15; median –0.98) models (Fig. S1C). Dependency aligned with oncogenic drivers: the *BRAF*
399 V600E-mutant BHT101 line was most sensitive (Chronos –1.15), followed by other *BRAF* V600E-
400 mutant lines (BCPAP, 8305C, 8505C), all showing high PDPK1 expression and strong
401 dependency (Table S4). PDPK1 expression correlated tightly with Chronos dependency ($r = 0.97$,
402 $p < 0.03$), reinforcing its functional relevance in thyroid cancer.

403 PDPK1 activity is regulated predominantly at the post-translational level; therefore,
404 messenger RNA (mRNA) or total protein abundance may not reliably reflect its functional status
405 (46). The critical activation step for PDPK1 is autophosphorylation at Ser241, which generates the
406 catalytically competent form required for downstream phosphorylation of AKT (Thr308), SGK,
407 and other AGC kinases. Because only the phosphorylated, active pool (p-PDPK1 S^{241}) propagates
408 PI3K/AKT signaling, quantifying this phosphorylated site provides a direct measure of pathway
409 engagement and oncogenic dependency. Therefore, we first characterized total and phospho-
410 PDPK1 in a panel of thyroid cancer cell lines. PDPK1 expression and phosphorylation varied in
411 the cell lines with known mutations in genes involved in the MAPK and PI3K/AKT pathways.
412 Cell lines harboring *PTEN* loss (FTC236, FTC133, and C643) and *BRAF* V600E mutations
413 (SW1736, 8505C, and BCPAP), as well as wild-type *BRAF* cell lines (THJ29T and C643) and a
414 *PIK3CA*-mutant/*MKRN1–BRAF* fusion cell line (THJ16T), all exhibited measurable PDPK1
415 expression (Fig. 1A). The phospho-PDPK1/PDPK1 ratio was markedly elevated in the FTC236,
416 C643, THJ16T, BCPAP, and 8505C cell lines relative to the HEK293 cell line (control), with the

417 THJ16T cell line demonstrating the highest PDPK1 phosphorylation, followed by the homozygous
418 *BRAF* V600E–mutant 8505C and BCPAP cell lines (Fig. 1A).
419 Consistent with MAPK pathway activation, all thyroid cancer cell lines evaluated showed
420 high MEK phosphorylation, with the *BRAF* V600E–mutant cell lines (BCPAP, 8505C, and
421 SW1736) exhibiting the highest phospho-MEK levels (Fig. 1A). The phospho-MEK/MEK ratio
422 was lower in the two patient-derived *BRAF* V600E–mutant ATC cell lines (ATC01 and ATC02)
423 compared to normal thyroid tissue, but total MEK levels were much higher in the patient-derived
424 ATC cell lines (Fig. 1B). The phospho-PDPK1/PDPK1 ratio was higher in the ATC02 cell line,
425 which was derived from a residual tumor resected after an exceptional response to combined Dab
426 and trametinib treatment, compared to the ATC01 cell line (derived tumor from a treatment-naïve
427 patient) or normal thyroid tissue. We used the *BRAF* V600E–mutant ATC cell lines (8505C and
428 SW1736) with relatively high and low phospho-PDPK1 levels and the patient-derived cell lines
429 (ATC01 and ATC02) to test the therapeutic efficacy of targeting PDPK1.
430
431 **Combined PDPK1 and BRAF V600E inhibition has synergistic anticancer activity *in vitro***
432 **and *ex vivo***
433 We evaluated drug response data from our previous drug screening studies for PDPK1
434 inhibitors in three ATC cell lines (8505C, THJ-11T, and THJ-16T), where BX795 emerged as the
435 most consistent and broadly active compound based on a half-maximal activity concentration
436 (AC_{50}) < 10 μM and **a** curve class up to –2.2. BX795 was the only agent to meet the criteria in all
437 three ATC cell lines, whereas BX-912, OSU-03012, and GSK-2334470 met the criteria in two
438 ATC cell lines, and DTXSID90678515 met the criteria in one ATC cell line (Fig. S1D). Therefore,
439 we used BX795 to inhibit PDPK1 phosphorylation. In addition, Integrated DepMap PRISM
440 analyses indicated that thyroid cancer cells are sensitive to BX795 treatment (Fig. S1E), further

441 supporting that the PDPK1 gene is essential. BX795 treatment significantly inhibited cell
442 proliferation in *BRAF* V600E–mutant ATC cell lines in a dose-dependent manner (Fig. 1C).
443 BX795 treatment reduced phosphorylation of PDPK1 at Ser241 and PI3KAKT/mTOR signaling,
444 with reduced S6K levels and upregulation of H_2AX phosphorylation (Fig. S1F). To further validate
445 the essentiality of PDPK1 and specificity of BX795 treatment, we knocked down PDPK1
446 expression. PDPK1 knockdown reduced total and phospho-PDPK1, changes associated with
447 inhibition of cellular proliferation (Fig. S1G). When combined with BX795 treatment to inhibit
448 PDPK1 phosphorylation at Ser241, there was further inhibition of cell proliferation compared to
449 the control (Fig. S1G). Collectively, the DepMap datasets and *in vitro* results suggest that targeting
450 PDPK1 for ATC therapy is a promising approach, especially in *BRAF* V600E–mutant ATC, where
451 resistance to combined BRAF and MEK inhibition is common.

452 PDPK1 inhibition with BX795 and BRAF V600E inhibition with Dab alone inhibited ATC
453 cellular proliferation (Fig. 1C–F). Combination BX795 and Dab treatment showed a synergistic
454 antiproliferative effect in *BRAF* V600E–mutant ATC cell lines at multiple dose combinations (Fig.
455 1G–J) based on a CI < 1. We selected combination concentrations (2.5 μM BX795 and 2.5 μM
456 Dab) that were synergistic and clinically achievable for the follow-up studies. Combination BX795
457 and Dab treatment significantly inhibited the size and number of ATC colonies and cellular
458 migration (Figs. 1K–N and S1H–I) compared to either agent alone or the vehicle control. BX795
459 alone and combination BX795 and Dab treatment in patient-derived *BRAF* V600E–mutant ATC
460 cells also significantly inhibited cellular proliferation (Fig. 1O–R).

461 We next tested the anticancer activity of combination BX795 and Dab treatment in *ex vivo*
462 (3D culture) model of *BRAF* V600E–mutant ATC cell lines (8505C and SW1736) and two patient-
463 derived *BRAF* V600E–mutant ATC cells (ATC01 and ATC02) that better recapitulate the
464 molecular features of human ATC and response to treatment. Dab treatment alone reduced the

465 spheroid size by ~72% (8505C) and ~56% (SW1736), and BX795 treatment alone reduced the
466 spheroid size by ~78% (8505C) and ~40% (SW1736) compared to the vehicle control;
467 combination treatment reduced the spheroid size significantly more than either agent alone (Fig.
468 1S–T). Similarly, in patient-derived ATC01 and ATC02 spheroids, combination treatment reduced
469 the spheroid size significantly more than either agent alone or the vehicle control (Fig. 1S–T).
470

471 **Combined PDPK1 and BRAF V600E inhibition has anticancer activity and is safe in *in vivo***
472 **orthotopic model of ATC**

473 We next tested combination BX795 and Dab treatment in an orthotopic mouse model using
474 the ATC *BRAF* V600E–mutant 8505C ATC cell line. BX795 and Dab treatment alone reduced the
475 tumor volume by 18% and 39%, respectively, compared to the vehicle control, whereas
476 combination BX795 and Dab treatment reduced the tumor volume by 55% compared to the vehicle
477 control (Figs. 2A and S2A–B). Combination BX795 and Dab treatment also significantly reduced
478 the tumor weight compared to the vehicle control in both genders (Fig. 2B; S2C-D). The total body
479 tumor luminescence measurement was significantly lower after treatment for 2 weeks, and the
480 growth rate was lower for the combination BX795 and Dab treatment group compared to the
481 vehicle control. Moreover, there were no metastases in any of the treatment groups (Fig. 2C–D).
482 There was no statistically significant difference in mouse weight among treatment groups, and
483 there were no treatment-related toxicities (Fig. 2E).
484

485 **Combined PDPK1 and BRAF V600E inhibition induces apoptosis**

486 To investigate the mechanism of the synergistic anticancer activity of combined PDPK1
487 and BRAF V600E inhibition, we performed TMT-based, label-intensity proteomic analysis with
488 BX795, Dab, or combination treatment. The results showed distinct pathway-selective effects with

489 monotherapy and a synergistic signaling convergence with combination treatment. Volcano plot
490 analysis demonstrated that BX795 treatment preferentially suppressed proteins involved in
491 PDPK1/AKT/mTOR signaling, ribosomal biogenesis, mitochondrial regulators, and cytoskeletal
492 organization, while inducing checkpoint- and stress-associated regulators (Fig. 3A). In contrast,
493 Dab treatment predominantly repressed MAPK-dependent proliferative and mitotic programs,
494 with compensatory activation of nuclear structural and transcriptional related proteins (Fig. 3B).
495 Combination treatment produced the greatest magnitude and breadth of proteomic remodeling,
496 marked by strong suppression of epithelial–mesenchymal transition (EMT)/metastasis-associated
497 proteins, translational machinery, and chromatin regulators, together with induction of DNA
498 damage, mitotic spindle destabilization, and apoptotic execution factors, consistent with mitotic
499 catastrophe (Fig. 3C). Venn diagram analysis revealed a conserved core of 134 shared total
500 proteins and 104 shared phosphoproteins across all three treatment groups, defining a common
501 stress-adaptive signaling module, while combination treatment uniquely altered 108 total proteins
502 and 40 phosphoproteins, indicating novel vulnerabilities unmasked only under dual pathway
503 inhibition (Fig. 3D). At the signaling level, phosphoproteomic analysis confirmed that BX795
504 suppressed PI3K/AKT/mTOR-dependent phosphorylation, Dab inhibited MEK/ERK and mitotic
505 phospho-networks, and combination treatment resulted in simultaneous shutdown of both
506 pathways, eliminating compensatory feedback upregulation. GSEA further demonstrated that
507 BX795 negatively enriched the PI3K/AKT/mTOR, mitotic spindle, oxidative phosphorylation,
508 WNT/β-catenin, and DNA repair pathways, while activating G2/M checkpoint inflammatory stress
509 and MAPK signaling. Dab suppressed MAPK-driven mitotic and metabolic programs with
510 activation of DNA repair, G2M checkpoints, EMT, p53, and oxidative phosphorylation checkpoint
511 pathways (Fig. 3E–F). Strikingly, combination treatment produced the most profound pathway-
512 level effects, with coordinated suppression of PI3K/AKT/mTOR, MAPK, WNT, mitosis,

513 oxidative phosphorylation, and DNA repair, alongside enrichment of p53, G2/M checkpoint, and
514 inflammatory response pathways, and repression of EMT signaling (Fig. 3G). Collectively, these
515 data establish that dual PDPK1 and BRAF V600E inhibition drives a synergistic, multi-layered
516 inhibition of survival, translational, cytoskeletal, mitotic, metabolic, and DNA repair networks,
517 leading to cell death.

518 To validate the proteomic results, we analyzed the canonical signaling pathways targeted
519 by BX795 and Dab, and cell death pathways. As expected, Dab reduced MEK phosphorylation,
520 and BX795 reduced PDPK1 phosphorylation at Ser^{241} (Fig. 3H). There was compensatory increase
521 in AKT^{308} + $PDPK1^{241}$ phosphorylation and MEK phosphorylation with BRAF V600E inhibition
522 alone and PDPK1 inhibition alone, respectively, but not with combined PDPK1 and BRAF V600E
523 inhibition, confirming dual pathway blockade (Fig. 3H).

524 In addition, combination PDPK1 and BRAF V600E inhibition significantly increased
525 apoptosis compared to either agent along and the vehicle control, with increased cleaved CASP3,
526 PARP-1 cleavage, decreased BCL-2, and enhanced AnnexinV/PI staining (Figs. 3H–I and S3A).
527 Furthermore, combination treatment reduced BAD phosphorylation and increased the active
528 BAD/inactive pBAD ratio by 3.4-fold and 2.4-fold in the 8505C and 2 SW1736 ATC cell lines,
529 respectively (Fig. 3J). Immunoprecipitation analysis revealing increased BCL-xL–BAD binding,
530 indicating BAD-mediated inhibition of BCL-xL's antiapoptotic function (Fig. 3K) with no binding
531 to BCL2. Furthermore, BX795 treatment reduced Ser^{9} phosphorylation (inactive) and increased
532 active GSK-3β levels, which were further enhanced with combination treatment (Fig. 3J). In
533 addition, combination PDPK1 and BRAF V600E inhibition increased γ-H2AX (Ser^{139}), indicating
534 greater DNA damage than with either agent alone and the vehicle control (Fig. 3J). Overall,
535 supervised cluster analysis demonstrated treatment-specific differential abundance across extrinsic
536 death receptor components (TNFRSF10A and FAS), mitochondrial apoptosis regulators (BAD,

537 BID, BAX, BAK1, and BCL2L1), and executioners of apoptosis (CASP3, CASP7, CASP8, and
538 CASP9), with a distinct expression signature including BAD, BAX, BCL2, CASP3, and PARP1
539 observed with combination treatment (Fig. 3L). Combination treatment led to higher levels of BID,
540 CASP3, and BAD and lower levels of BCL2L1 and PARP1. Although the total BAX and BCL2
541 protein levels were lower, the BAX/BCL2 ratio was high after combination treatment compared
542 to either agent alone, further supporting enhanced apoptosis (Fig. 3L), Together, these results show
543 that combination treatment synergistically induces apoptosis, activates caspase, leads to DNA
544 damage, and suppresses survival signaling pathways in *BRAF* V600E–mutant ATC cells.
545

546 **Combination BX795 and Dab treatment induces DNA damage and G2 cell cycle arrest in**
547 **ATC cells**

548 To assess DNA damage induced by combination treatment, we evaluated the formation of
549 γH2AX (Ser139) foci. Both BX795 and Dab treatment alone increased γH2AX, with combination
550 treatment resulting in the highest number of foci, γH2AX-positive cells, and fluorescence intensity
551 (Fig. 3M). Furthermore, DNA damage response activation was highest with combination
552 treatment, with a greater increase in ATM (Ser^{1981}) and CHK2 (T^{68}) phosphorylation, while CHK1
553 (Ser^{345}) phosphorylation increased with Dab treatment, decreased with BX795 treatment, and had
554 an intermediate effect with combination treatment (Fig. 3N).

555 Cell cycle analysis showed BX795 induced strong G2/M arrest, Dab caused G0/G1 arrest,
556 and combination treatment significantly increased G2/M arrest with 4N DNA accumulation (Fig.
557 3O). BX795 increased cyclin B, which was further elevated with combination treatment, while
558 both agents alone reduced the CDK1/pCDK1 ratio, PLK1 phosphorylation, and phospho-CDC25C
559 (Thr^{48}), with the strongest effect observed with combination treatment (Fig. 3P). Combination
560 treatment also lowered cyclin A2 and depleted phospho-histone H3 (Ser^{10}), and disrupted spindle

561 microtubule assembly in nocodazole-synchronized cells, indicating failure to progress from the
562 G2 phase to the M phase despite cyclin B accumulation. Likewise, Dab treatment reduced cyclin
563 D1, which was further reduced with combination treatment due to proteasomal degradation;
564 however, BX795 treatment alone had no effect (Fig. 3Q). Together, these data demonstrate that
565 combined PDPK1 and BRAF inhibition synergistically disrupts cell-cycle progression by
566 enforcing G2/M arrest with defective mitotic entry, accompanied by proteasomal degradation of
567 cyclin D1.

568 We further assessed DNA damage responses associated with combination treatment–
569 induced G2 arrest based on the phosphoproteomic results. Combination treatment resulted in the
570 highest phosphorylation of RAD50, CDK1, MCM2, PRKDC, and XRCC5 compared with either
571 agent alone (Fig. 3R), consistent with enhanced sensing of double-stranded DNA (dsDNA) breaks,
572 replication stress, reinforced G2/M checkpoint activation, and increased engagement of non-
573 homologous end joining (NHEJ)-mediated repair. In contrast, combination treatment reduced the
574 abundance of LIG1, MDC1, and MSH6 relative to treatment with either agent alone, indicating
575 suppression of DNA repair synthesis, chromatin-based damage signaling, and mismatch repair
576 pathways (Fig. 3R). Together, these findings indicate that combination treatment leads to a greater
577 DNA damage burden marked by replication stress, checkpoint activation, and NHEJ engagement,
578 while suppressing key DNA repair scaffolding and mismatch repair components.

579 Taken together, these findings suggest that dual PDPK1 and BRAF V600E inhibition
580 activates ATM/CHK2 signaling, downregulates G2/M regulators, blocks mitotic entry, and
581 enforces persistent G2 arrest in ATC cells.

582

583 **Combination BX795 and Dab treatment induces mitotic G2 arrest that is associated with**
584 **mitochondrial dysfunction**

585 Given that prolonged cell cycle arrest can result in oxidative stress, we assessed ROS levels
586 following treatment with BX795, Dab, or their combination in *BRAF* V600E–mutant ATC cells.
587 Combination treatment markedly increased intracellular ROS (DCFH-DA) and mitochondrial
588 superoxide (MitoSOX) compared with either agent alone or the vehicle control (Fig. 4A–B).
589 MitoTracker Green staining revealed increased mitochondrial content that was most pronounced
590 with combination treatment (Fig. 4C–D), accompanied by a higher mitochondrial membrane
591 potential (TMRM) without loss of integrity (Fig. 4E).

592 Seahorse analysis showed that combination treatment significantly reduced basal, ATP-
593 linked, and maximal respiration, indicating impairment in oxidative phosphorylation (Figs. 4F and
594 S4A). Mitochondrial integrity was also confirmed by JC-1 staining (Fig. S4B). Profiling of
595 proteins related to oxidative phosphorylation revealed complex, specific changes with combined
596 treatments, where complex V increased in both *BRAF* V600E–mutant ATC cell lines. On the other
597 hand, relative to the vehicle control, complex III was higher in 8505C cells, while complex II and
598 IV were higher in SW1736 cells (Fig. S4C).

599 We performed supervised cluster analysis of the proteomic data to determine the effect of
600 BX795, Dab, and their combination on proteins involved in mitochondrial ribosomal function,
601 electron transport chain complexes, the tricarboxylic acid (TCA) cycle, mitochondrial dynamics,
602 and metabolite transport (Fig. 5G). We found higher relative abundance of mitochondrial
603 respiratory chain and metabolic enzymes with BX795 treatment, including multiple complex I
604 subunits (NDUFS1, NDUFS7, NDUFS2, NDUFS3, NDUFV1, and NDUFB8), complex II
605 components (SDHA, SDHB, SDHC, and SDHD), complex III proteins (UQCRC1 and UQCRC2),
606 complex IV subunits (COX5A, COX4I1, COX6C, COX7C, COX5B, and COX7A2), and ATP
607 synthase subunits (ATP5F1A, ATP5F1B, ATP5F1C, ATP5PB, and ATP5PF). There was reduced
608 relative abundance with Dab treatment and markedly reduced abundance with combination

609 treatment. Proteins involved in the TCA cycle and mitochondrial metabolism, including IDH1,
610 IDH2, IDH3A, IDH3B, FH, OGDH, DLST, MDH2, CS, PDHA1, PDHB, PC, DLD, GLUD1,
611 ACADM, and ACADVL, followed a similar pattern, with higher expression with BX795
612 treatment, intermediate or reduced expression with Dab treatment, and the lowest relative
613 abundance with combination treatment.

614 Mitochondrial structure, dynamics, and transport proteins, including TFAM, TOMM20,
615 TIMM23, MFN1, OPA1, DNM1L, VDAC1, VDAC2, and VDAC3, also a demonstrated
616 progressive reduction from BX795 to Dab treatment, and a further reduction with combination
617 treatment. CYCS and HSPA9 displayed higher abundance with BX795 treatment, reduced
618 abundance with Dab treatment, and further reduction with combination treatment. Collectively,
619 these data demonstrate broad and coordinated suppression of mitochondrial oxidative
620 phosphorylation, TCA cycle activity, and mitochondrial structural components with combination
621 treatment, with intermediate effects observed with Dab treatment alone and the highest relative
622 expression with BX795 treatment.

623 The consistent decrease in mitochondrial complex proteins supports that mitochondrial
624 dysfunction occurs with dual PDPK1 and BRAF V600E inhibition. This triggers ROS generation
625 even though the mitochondrial membrane potential is preserved. These changes are consistent with
626 a glycolytic, senescence-like phenotype as described previously (47).

627

628 **ROS scavenging mitigates genotoxicity while CHK2 inhibition induces mitotic slippage and**
629 **partially reverses combination therapy-induced apoptosis**

630 Next, we preformed time-course analysis to determine the sequence of events with
631 combination treatment that leads to its synergistic anticancer activity. We found G2/M arrest
632 occurred by 6 h; this preceded ROS elevation (which began at 12 h) (Fig. 5A–B). The

633 mitochondrial membrane potential increased as early as 6 h, while mitochondrial accumulation
634 occurred later (≥ 20 h) (Fig. S4D–E). Thus, combination treatment induces early G2/M arrest and
635 mitochondrial hyperpolarization, followed by sustained ROS production in *BRAF* V600E–mutant
636 ATC cells. To assess the role of ROS in combination treatment–induced cytotoxicity, we used the
637 ROS scavengers *N*-acetyl cysteine (NAC) and MitoQ. NAC significantly reduced combination
638 treatment–induced ROS (DCFH-DA) (Fig. 5C), apoptosis (Annexin V/PI) (Fig. 5D), and PARP
639 cleavage (Fig. 5E), indicating ROS-mediated apoptosis. NAC treatment also decreased γ-H_2AX
640 and DNA damage response proteins (pATM and pCHK2) but did not reverse G2 arrest (Fig. S4F),
641 suggesting ROS generation occurs downstream of cell cycle arrest. MitoQ treatment partially
642 released cells from G2 arrest (Fig. 5F), implicating mitochondrial superoxide in cell cycle
643 regulation.

644 Next, to explore the involvement of CHKs in combination treatment–induced cell cycle
645 arrest, we used the CHK2 inhibitor BML-277, which significantly reversed combination
646 treatment–induced G2 arrest (Figs. 5G and S4G), cell proliferation (Fig. 5H), and apoptosis (Fig.
647 5I) in 8505C cells. As CHK1 and CHK2 both were active in SW1736 cells, we used AZD7762
648 (which inhibits both CHK1 and CHK2) in SW1736 cells, which resulted in mitotic slippage (Fig.
649 S4H) and reversed the inhibition of cellular proliferation (Fig. S4I). These data suggest that mitotic
650 arrest leads to apoptosis, which can be partially reversed by mitotic slippage.

651

652 **DISCUSSION**

653 PDPK1 is overexpressed in thyroid cancer (39). High PDPK1 levels in thyroid cancer are
654 associated with advanced stage, larger tumor size, lymph node metastasis, ATC, and worse overall
655 and recurrence-free survival (48). In this study, we found high levels of total and phosphorylated
656 PDPK1 at Ser241 in ATC cells, and combined inhibition of PDPK1 and BRAF V600E had

657 synergistic anticancer activity in *BRAF* V600E–mutant ATC in *in vitro*, *ex vivo*, and *in vivo*
658 models. Mechanistically, this combination effectively suppressed both the PDPK1/AKT and
659 MAPK pathways without rebound activation that is seen with inhibition of a single pathway. Dual
660 inhibition resulted in pronounced DNA damage, G2 cell cycle arrest, and apoptosis in *BRAF*
661 V600E–mutant ATC cells.

662 Dual inhibition of PDPK1 and mutant *BRAF* V600E–mutant ATC drives accumulation of
663 dsDNA damage and G2 arrest through complementary mechanisms, where *BRAF* V600E
664 inhibition induces replication stress by abruptly halting MAPK-driven proliferation, generating
665 stalled replication forks that can collapse into dsDNA breaks (49). PDPK1 blockade suppresses
666 AKT and other AGC kinase signaling, impairing key DNA repair pathways including homologous
667 recombination and NHEJ, thereby preventing resolution of these molecular events (50,51). The
668 resulting accumulation of unrepaired DNA damage activates the G2/M checkpoint, enforcing cell
669 cycle arrest and sensitizing cells to apoptosis (52). We found the combined inhibition of PDPK1
670 and *BRAF* V600E results in accumulation of unrepaired DNA damage, which activates the G2/M
671 checkpoint and enhances apoptotic commitment, as observed in our cell viability and apoptosis
672 assays. Interestingly, this genotoxic stress is also accompanied by mitochondrial dysfunction,
673 characterized by disrupted oxidative phosphorylation and an unexpected increase in the
674 mitochondrial membrane potential, without triggering mitochondrial outer membrane
675 permeabilization. This hyperpolarized mitochondrial state likely reflects an adaptive response to
676 maintain ATP production under DNA damage–induced metabolic stress, consistent with previous
677 observations that DNA damage can alter mitochondrial bioenergetics and promote mitochondrial
678 hyperpolarization (53,54). This mechanistic interplay aligns with studies linking cell cycle
679 checkpoint disruption to mitochondrial dysfunction, ROS accumulation, and apoptotic priming
680 (55).

681 Treatment with the mitochondria-targeted antioxidant MitoQ partially reduced G2 arrest,
682 suggesting that mitochondrial ROS and hyperpolarization contribute to the enforcement of cell
683 cycle checkpoints. This is consistent with reports that mitochondrial ROS can act as signaling
684 intermediates to activate DNA damage checkpoints and maintain G2 arrest (53,56). These findings
685 imply that mitochondrial bioenergetic stress is not merely a byproduct of DNA damage but
686 actively reinforces G2/M checkpoint signaling. Therapeutically, this highlights that combined
687 inhibition of PDPK1 and BRAF V600E exploits a dual vulnerability: suppression of proliferative
688 signaling and engagement of DNA damage responses. These results highlight a feed-forward
689 mechanism where mitochondrial dysfunction amplifies cell cycle arrest, providing a therapeutic
690 vulnerability that is exploitable by combined inhibition of PDPK1 and BRAF V600E.

691 Dual inhibition of PDPK1 and *BRAF* V600E promoted dsDNA breaks and oxidative stress.
692 Notably, treatment with the ROS scavenger NAC attenuated apoptosis and reduced DNA damage
693 but did not reverse G2 arrest, indicating that mitochondrial ROS primarily function downstream
694 of cell cycle checkpoint activation to drive cell death rather than initiating the arrest itself. NAC
695 primarily scavenges H_2O_2, HOCl, and •OH, increasing GSH levels (57), whereas MitoQ targets
696 mitochondrial superoxide and H_2O_2 (58). Because ROS species can propagate via chain reactions
697 (59,60), MitoQ-mediated arrest release supports a role for mitochondrial superoxide in sustaining
698 G2 arrest during combination treatment. These findings suggest a model in which DNA damage
699 response–mediated G2 arrest primes mitochondria toward a hyperpolarized, pro-apoptotic state,
700 with oxidative stress acting as a critical amplifier of apoptosis in ATC cells (53,56). Although the
701 OCR was not reduced, mitochondrial hyperpolarization reflects impaired proton dissipation and
702 electron congestion within the electron transport chain rather than enhanced oxidative
703 phosphorylation, a characteristic feature of dysfunctional, ROS-producing mitochondria (61).
704 BAD phosphorylation by AKT and RSK1—regulated by PDPK1 and MAPK—leads to

705 inactivation and sequestration by 14-3-3 proteins, a mechanism linked to BRAF inhibitor
706 resistance in melanoma (62). Inhibiting PI3K/PDPK1/AKT and BRAF pathways prevents BAD
707 sequestration and promotes active BAD driven apoptosis (63–65). This mechanism underscores
708 the therapeutic potential of combining PDPK1 and BRAF V600E inhibition to simultaneously
709 enforce cell cycle blockade and trigger ROS-dependent apoptotic pathways.

710 ATC harbors frequent mutations in genes that lead to activation of both the
711 PI3K/AKT/mTOR and MAPK signaling pathways. Activating mutations in PIK3CA occur in
712 approximately 10%–20% of ATC cases, while PTEN loss or inactivating mutations are also
713 common, collectively promoting constitutive PI3K/AKT signaling (4,66,67). In parallel, MAPK
714 pathway activation is highly prevalent, with *BRAF* V600E mutations detected in 40%–70% of
715 ATC cases, and RAS mutations contributing to MAPK hyperactivation in a significant subset
716 (4,68). These two pathways are activated in ATC, reinforcing proliferative, survival, and stress-
717 adaptive signaling. Their combined deregulation underpins therapeutic resistance to *BRAF* V600E
718 inhibitors and a poor prognosis in ATC (63,69,70), underscoring the need for rational dual-
719 targeting strategies. PDPK1 represents a strategic therapeutic node in ATC because it lies
720 downstream of PI3K and integrates signals from multiple recurrent alterations, including *PIK3CA*,
721 *PTEN*, and *RAS*. Selective inhibition of PI3K or AKT may leave bypass pathways intact. On the
722 other hand, PDPK1 activates a broad network of AGC kinases (AKT, SGK, S6K, and PKC
723 isoforms), making it a more effective point of signaling blockade. By targeting PDPK1, both
724 survival signaling and stress-adaptation programs are disrupted, addressing the multifaceted
725 oncogenic landscape of ATC.

726 The therapeutic implications of our findings are immediate. Dab is a Food and Drug
727 Administration–approved inhibitor of BRAF V600E, while the PDPK1 inhibitor BX795 has
728 antitumor activity in *in vitro*, *ex vivo*, and *in vivo* models of ATC and resulted in no treatment-

729 related toxicity alone or in combination with Dab *in vivo*. Our data show that PDPK1 inhibition
730 exerts intrinsic anticancer activity and significantly enhances BRAF V600E inhibition, supporting
731 a rational, dual-targeted approach. Given that both compounds have been validated preclinically
732 and/or clinically, this combination represents an opportunity to translate this combination into an
733 early-phase clinical trial in *BRAF* V600E–mutant ATC. Moreover, because *BRAF* V600E is
734 present in ~15% of all human cancers, this strategy may extend beyond ATC to other malignancies
735 driven by MAPK and PI3K/AKT/mTOR crosstalk.

736 In summary, we have identified PDPK1 as a critical therapeutic vulnerability in ATC. By
737 functioning as a central effector of PI3K/AKT/mTOR signaling, PDPK1 integrates multiple
738 oncogenic inputs common in ATC, and its inhibition disrupts both survival and stress-adaptation
739 pathways. Importantly, combining PDPK1 inhibition with BRAF blockade yields synergistic
740 anticancer activity. These findings provide a strong rationale for advancing PDPK1 inhibition,
741 particularly in combination with *BRAF* V600E inhibition, into the clinic.

742

743 **Funding declaration**

744 Early drug screening work was supported through the National Cancer Institute, National
745 Institutes of Health (ZIABC011286-09). The remainder of the research was supported through the
746 Stanford Medicine Harry A. Oberhelman Jr. and Mark L. Welton endowment at Stanford
747 University.

748

749 **Author Contribution declaration**

750 Tejinder Pal Khaket: Conceptualization, Methodology, Validation, Investigation, Visualization,
751 Writing- Original draft preparation. Chandrayee Ghosh, Zhongyue Yang, Jiangnan Hu, Eden D.
752 Alamaw, Myriem Boufraqech, Thorkell Andresson Maura O'Neill, Ya-Qin Zhang, Min Shen,

Bereketeab Haileselassie: Visualization, Investigation, Data curation, Methodology. Electron Kebebew: Supervision, Conceptualization, Project administration, Writing- Reviewing and Editing, Funding acquisition.

Declaration of Competing Interest

The authors declare that they have no known competing financial interests or personal relationships that could have appeared to influence the work reported in this paper.

Consent to Publish declaration: Not applicable

Ethics Approval and Consent to Participate

Patient-derived tumor samples were obtained under protocols approved by the Stanford University Institutional Review Board (IRB protocol 50782). All samples were collected with written informed consent from participants in accordance with institutional guidelines. No identifying information was used.

All animal procedures were approved by the Stanford Administrative Panel on Laboratory Animal Care (APLAC; Protocol #34767) and conducted in accordance with institutional and federal guidelines.

Availability of data and materials: All data generated or analyzed during this study are presented within the manuscript and its supplementary materials. Any additional information or raw datasets can be obtained from the corresponding author upon reasonable request.

References

777 1. Kebebew E, Greenspan FS, Clark OH, Woeber KA, McMillan A. Anaplastic thyroid
778 carcinoma. Treatment outcome and prognostic factors. Cancer 2005;103:1330–5.
779 2. Nilubol N, Kebebew E. Should small papillary thyroid cancer be observed? A
780 population-based study. Cancer 2015;121:1017–24.
781 3. Bible KC, Kebebew E, Brierley J et al. 2021 American Thyroid Association Guidelines
782 for management of patients with anaplastic thyroid cancer. Thyroid 2021;31:337–86.
783 4. Landa I, Ibrahimpasic T, Boucai L et al. Genomic and transcriptomic hallmarks of poorly
784 differentiated and anaplastic thyroid cancers. J Clin Invest 2016;126:1052–66.
785 5. Tiedje V, Ting S, Herold T et al. NGS based identification of mutational hotspots for
786 targeted therapy in anaplastic thyroid carcinoma. Oncotarget 2017;8:42613–20.
787 6. Feldman RI, Wu JM, Polokoff MA et al. Novel small molecule inhibitors of 3-
788 phosphoinositide-dependent kinase-1. J Biol Chem 2005;280:19867–74.
789 7. Subbiah V, Kreitman RJ, Wainberg ZA et al. Dabrafenib and trametinib treatment in
790 Patients with locally advanced or metastatic BRAF V600-mutant anaplastic thyroid
791 cancer. J Clin Oncol 2018;36:7–13.
792 8. Wang VE, Xue JY, Frederick DT et al. Adaptive resistance to dual BRAF/MEK
793 inhibition in BRAF-driven tumors through autocrine FGFR pathway activation. Clin
794 Cancer Res 2019;25:7202–17.
795 9. Montero-Conde C, Ruiz-Llorente S, Dominguez JM et al. Relief of feedback inhibition of
796 HER3 transcription by RAF and MEK inhibitors attenuates their antitumor effects in
797 BRAF-mutant thyroid carcinomas. Cancer Discov 2013;3:520–33.
798 10. Xu B, Fuchs T, Dogan S et al. Dissecting anaplastic thyroid carcinoma: A comprehensive
799 clinical, histologic, immunophenotypic, and molecular study of 360 cases. Thyroid
800 2020;30:1505–17.

801 11. Kandil E, Tsumagari K, Ma J et al. Synergistic inhibition of thyroid cancer by
802 suppressing MAPK/PI3K/AKT pathways. J Surg Res 2013;184:898–906.
803 12. Castellano E, Downward J. RAS interaction with PI3K: More than just another effector
804 pathway. Genes Cancer 2011;2:261–74.
805 13. Chi M, Ye Y, Zhang XD, Chen J. Insulin induces drug resistance in melanoma through
806 activation of the PI3K/Akt pathway. Drug Des Devel Ther 2014;8:255–62.
807 14. Jiang CC, Lai F, Thorne RF et al. MEK-independent survival of B-RAFV600E
808 melanoma cells selected for resistance to apoptosis induced by the RAF inhibitor
809 PLX4720. Clin Cancer Res 2011;17:721–30.
810 15. Byeon HK, Na HJ, Yang YJ et al. Acquired resistance to BRAF inhibition induces
811 epithelial-to-mesenchymal transition in BRAF (V600E) mutant thyroid cancer by c-Met-
812 mediated AKT activation. Oncotarget 2017;8:596–609.
813 16. Byeon HK, Na HJ, Yang YJ et al. c-Met-mediated reactivation of PI3K/AKT signaling
814 contributes to insensitivity of BRAF(V600E) mutant thyroid cancer to BRAF inhibition.
815 Mol Carcinog 2016;55:1678–87.
816 17. Guo H, German P, Bai S et al. The PI3K/AKT pathway and renal cell carcinoma. J Genet
817 Genomics 2015;42:343–53.
818 18. Gagliardi PA, Puliafito A, Primo L. PDK1: At the crossroad of cancer signaling
819 pathways. Semin Cancer Biol 2018;48:27–35.
820 19. Dangelmaier C, Manne BK, Liverani E, Jin J, Bray P, Kunapuli SP. PDK1 selectively
821 phosphorylates Thr(308) on Akt and contributes to human platelet functional responses.
822 Thromb Haemost 2014;111:508–17.

823 20. Zabkiewicz J, Pearn L, Hills RK et al. The PDK1 master kinase is over-expressed in
824 acute myeloid leukemia and promotes PKC-mediated survival of leukemic blasts.
825 Haematologica 2014;99:858–64.
826 21. Pearn L, Fisher J, Burnett AK, Darley RL. The role of PKC and PDK1 in monocyte
827 lineage specification by Ras. Blood 2007;109:4461–9.
828 22. Maurer M, Su T, Saal LH et al. 3-Phosphoinositide-dependent kinase 1 potentiates
829 upstream lesions on the phosphatidylinositol 3-kinase pathway in breast carcinoma.
830 Cancer Res 2009;69:6299–306.
831 23. Du J, Yang M, Chen S, Li D, Chang Z, Dong Z. PDK1 promotes tumor growth and
832 metastasis in a spontaneous breast cancer model. Oncogene 2016;35:3314–23.
833 24. Lohneis P, Darb-Esfahani S, Dietel M, Braicu I, Sehouli J, Arsenic R. PDK1 is expressed
834 in ovarian serous carcinoma and correlates with improved survival in high-grade tumors.
835 Anticancer Res 2015;35:6329–34.
836 25. Ahmed N, Riley C, Quinn MA. An immunohistochemical perspective of PPAR beta and
837 one of its putative targets PDK1 in normal ovaries, benign and malignant ovarian
838 tumours. Br J Cancer 2008;98:1415–24.
839 26. Choucair KA, Guerard KP, Ejdelman J et al. The 16p13.3 (PDPK1) genomic gain in
840 prostate cancer: A potential role in disease progression. Transl Oncol 2012;5:453–60.
841 27. Jiang Q, Zheng N, Bu L et al. Correction: SPOP-mediated ubiquitination and degradation
842 of PDK1 suppresses AKT kinase activity and oncogenic functions. Mol Cancer
843 2025;24:137.
844 28. Scortegagna M, Ruller C, Feng Y et al. Genetic inactivation or pharmacological
845 inhibition of Pdk1 delays development and inhibits metastasis of Braf(V600E)::Pten(-/-)
846 melanoma. Oncogene 2014;33:4330–9.

847 29. Emmanouilidi A, Fyffe CA, Ferro R et al. Preclinical validation of 3-phosphoinositide-
848 dependent protein kinase 1 inhibition in pancreatic cancer. J Exp Clin Cancer Res
849 2019;38:191.
850 30. Casari I, Domenichini A, Sestito S et al. Dual PDK1/aurora kinase A inhibitors reduce
851 pancreatic cancer cell proliferation and colony formation. Cancers (Basel) 2019;11.
852 31. Wu N, He C, Zhu B, Jiang J, Chen Y, Ma T. 3-Phosphoinositide dependent protein
853 kinase-1 (PDK-1) promotes migration and invasion in gastric cancer cells through
854 activating the NF-kappaB pathway. Oncol Res 2017;25:1153–59.
855 32. Bai X, Li P, Xie Y et al. Overexpression of 3-phosphoinositide-dependent protein kinase-
856 1 is associated with prognosis of gastric carcinoma. Tumour Biol 2016;37:2333–9.
857 33. Wang J, Liu F, Ao P et al. Correlation of PDK1 expression with clinicopathologic
858 features and prognosis of hepatocellular carcinoma. Onco Targets Ther 2016;9:5597–
859 602.
860 34. Yang Z, Wu Z, Liu T et al. Upregulation of PDK1 associates with poor prognosis in
861 esophageal squamous cell carcinoma with facilitating tumorigenicity in vitro. Med Oncol
862 2014;31:337.
863 35. Luo D, Xu X, Li J et al. The PDK1/c-Jun pathway activated by TGF-beta induces EMT
864 and promotes proliferation and invasion in human glioblastoma. Int J Oncol
865 2018;53:2067–80.
866 36. Jing P, Zhou S, Xu P et al. PDK1 promotes metastasis by inducing epithelial-
867 mesenchymal transition in hypopharyngeal carcinoma via the Notch1 signaling pathway.
868 Exp Cell Res 2020;386:111746.

869 37. Tang N, Hu B, Zhang Y, Chen Z, Yu R. Possible involvement of the Hedgehog and
870 PDPK1-Akt pathways in the growth and migration of small-cell lung cancer. J Int Med
871 Res 2021;49:3000605211016562.
872 38. Zhang X, Yu Z. Expression of PDK1 in malignant pheochromocytoma as a new
873 promising potential therapeutic target. Clin Transl Oncol 2019;21:1312–8.
874 39. Sun Z, Xu L. Expression of PDK-1 and DMBT1 in the thyroid carcinoma and its
875 clinicopathological significance. Oncol Lett 2019;18:2819–24.
876 40. Lin HJ, Hsieh FC, Song H, Lin J. Elevated phosphorylation and activation of PDK-
877 1/AKT pathway in human breast cancer. Br J Cancer 2005;93:1372–81.
878 41. Bamodu OA, Chang HL, Ong JR, Lee WH, Yeh CT, Tsai JT. Elevated PDK1 expression
879 drives PI3K/AKT/MTOR signaling promotes radiation-resistant and dedifferentiated
880 phenotype of hepatocellular carcinoma. Cells 2020;9.
881 42. Choi JH, Yang YR, Lee SK et al. Potential inhibition of PDK1/Akt signaling by
882 phenothiazines suppresses cancer cell proliferation and survival. Ann N Y Acad Sci
883 2008;1138:393–403.
884 43. Nagashima K, Shumway SD, Sathyanarayanan S et al. Genetic and pharmacological
885 inhibition of PDK1 in cancer cells: characterization of a selective allosteric kinase
886 inhibitor. J Biol Chem 2011;286:6433–48.
887 44. Ding L, Ren C, Yang L et al. OSU-03012 disrupts Akt signaling and prevents
888 endometrial carcinoma progression in vitro and in vivo. Drug Des Devel Ther
889 2021;15:1797–810.
890 45. Chou TC. Drug combination studies and their synergy quantification using the Chou-
891 Talalay method. Cancer Res 2010;70:440–6.

892 46. Bayascas JR, Wullschleger S, Sakamoto K et al. Mutation of the PDK1 PH domain
893 inhibits protein kinase B/Akt, leading to small size and insulin resistance. Mol Cell Biol
894 2008;28:3258–72.
895 47. Correia-Melo C, Marques FD, Anderson R et al. Mitochondria are required for pro-
896 ageing features of the senescent phenotype. EMBO J 2016;35:724–42.
897 48. Wang M, Mao C, Ouyang L et al. Pathological and prognostic role of PDK1 in papillary
898 thyroid carcinoma. Biochem Biophys Res Commun 2020;524:338–44.
899 49. Yang C, Tian C, Hoffman TE, Jacobsen NK, Spencer SL. Melanoma subpopulations that
900 rapidly escape MAPK pathway inhibition incur DNA damage and rely on stress
901 signalling. Nat Commun 2021;12:1747.
902 50. Fraser M, Harding SM, Zhao H, Coackley C, Durocher D, Bristow RG. MRE11
903 promotes AKT phosphorylation in direct response to DNA double-strand breaks. Cell
904 Cycle 2011;10:2218–32.
905 51. Toulany M, Lee KJ, Fattah KR et al. Akt promotes post-irradiation survival of human
906 tumor cells through initiation, progression, and termination of DNA-PKcs-dependent
907 DNA double-strand break repair. Mol Cancer Res 2012;10:945–57.
908 52. Stommel JM, Kimmelman AC, Ying H et al. Coactivation of receptor tyrosine kinases
909 affects the response of tumor cells to targeted therapies. Science 2007;318:287–90.
910 53. Zorov DB, Juhaszova M, Sollott SJ. Mitochondrial reactive oxygen species (ROS) and
911 ROS-induced ROS release. Physiol Rev 2014;94:909–50.
912 54. Wang X, Lim, HJ, Son YO. Down-regulation of mitochondrial voltage-dependent anion
913 channel (VDAC) contributes to protective effect of DNA damage on apoptosis. J Biol
914 Chem 2010;285:34960–70.

915 55. Raimundo N, Song L, Shutt TE et al. Mitochondrial stress engages E2F1 apoptotic
916 signaling to cause deafness. Cell 2012;148:716–26.
917 56. Srinivas US, Tan BWQ, Vellayappan BA, Jeyasekharan AD. ROS and the DNA damage
918 response in cancer. Redox Biol 2019;25:101084.
919 57. Pedre B, Barayeu U, Ezerina D, Dick TP. The mechanism of action of N-acetylcysteine
920 (NAC): The emerging role of H(2)S and sulfane sulfur species. Pharmacol Ther
921 2021;228:107916.
922 58. Sena LA, Chandel NS. Physiological roles of mitochondrial reactive oxygen species. Mol
923 Cell 2012;48:158–67.
924 59. Khaket TP, Ahmad R. Biochemical studies on hemoglobin modified with reactive
925 oxygen species (ROS). Appl Biochem Biotechnol 2011;164:1422–30.
926 60. Collin F. Chemical basis of reactive oxygen species reactivity and involvement in
927 neurodegenerative diseases. Int J Mol Sci 2019;20.
928 61. Brand MD, Nicholls DG. Assessing mitochondrial dysfunction in cells. Biochem J
929 2011;435:297–312.
930 62. Perna D, Karreth FA, Rust AG et al. BRAF inhibitor resistance mediated by the AKT
931 pathway in an oncogenic BRAF mouse melanoma model. Proc Natl Acad Sci U S A
932 2015;112:E536–45.
933 63. Scheid MP, Duronio V. Dissociation of cytokine-induced phosphorylation of Bad and
934 activation of PKB/akt: involvement of MEK upstream of Bad phosphorylation. Proc Natl
935 Acad Sci U S A 1998;95:7439–44.
936 64. She QB, Solit DB, Ye Q, O'Reilly KE, Lobo J, Rosen N. The BAD protein integrates
937 survival signaling by EGFR/MAPK and PI3K/Akt kinase pathways in PTEN-deficient
938 tumor cells. Cancer Cell 2005;8:287–97.

939 65. Fang X, Yu S, Eder A et al. Regulation of BAD phosphorylation at serine 112 by the
940 Ras-mitogen-activated protein kinase pathway. Oncogene 1999;18:6635–40.
941 66. Ricarte-Filho JC, Ryder M, Chitale DA et al. Mutational profile of advanced primary and
942 metastatic radioactive iodine-refractory thyroid cancers reveals distinct pathogenetic roles
943 for BRAF, PIK3CA, and AKT1. Cancer Res 2009;69:4885–93.
944 67. Pozdeyev N, Gay LM, Sokol ES et al. Genetic analysis of 779 advanced differentiated
945 and anaplastic thyroid cancers. Clin Cancer Res 2018;24:3059–68.
946 68. Xing M. Molecular pathogenesis and mechanisms of thyroid cancer. Nat Rev Cancer
947 2013;13:184–99.
948 69. Gowrishankar K, Snoyman S, Pupo GM, Becker TM, Kefford RF, Rizos H. Acquired
949 resistance to BRAF inhibition can confer cross-resistance to combined BRAF/MEK
950 inhibition. J Invest Dermatol 2012;132:1850–9.
951 70. Villanueva J, Vultur A, Lee JT et al. Acquired resistance to BRAF inhibitors mediated by
952 a RAF kinase switch in melanoma can be overcome by cotargeting MEK and IGF-
953 1R/PI3K. Cancer Cell 2010;18:683–95.
954
955
956
957
958
959
960
961
962

963 **Fig. 1: Combined PDPK1 and BRAF V600E inhibition has synergistic anticancer activity *in***
964 ***vitro* and *ex vivo*.**
965 (A) Immunobloting of pPDPK1, PDPK1, pMEK, and MEK in thyroid cancer lines: papillary
966 thyroid cancer (PTC, brown color) (TPC1), follicular thyroid cancer (FTC, blue color) (FTC-133
967 and FTC-236), poorly differentiated thyroid cancer (PDTC, green color) (BCPAP), *BRAF* wild
968 type anaplastic thyroid cancer (ATC) (red color) (C643 and THJ29T), *BRAF*V600E–mutant ATC
969 (8505C, SW1736, and THJ16T), and HEK293 cells using β-actin as a loading control. The relative
970 ratio of pPDPK1 to total PDPK1 and pMEK to total MEK is listed below each phospho-protein
971 compared to HEK293 cells. (B) Immunoblotting of phosphoPDPK1, total PDPK1 in untreated and
972 dabrafenib (Dab) and trametinib–treated patient derived ATC and normal thyroid tissues using β-
973 actin as a loading control. The relative ratio of pPDPK1 to total PDPK1 and pMEK to total MEK
974 is listed below each phospho-protein compared to normal thyroid tissue. (C–D) Dose-dependent
975 inhibition of cell proliferation with BX795 treatment in 8505C and SW1736 cells after 48 h. (E–
976 F) Dose-dependent inhibition of cell proliferation with Dab treatment in 8505C and SW1736 ATC
977 cells after 48 h. (G–H) Analysis of the combination index (CI) using the CompuSyn software for
978 BX795, Dab, and their combination in *BRAF* V600E–mutant ATC cell lines. CI < 1 indicates
979 synergism, and fa denotes fraction affected. (I–J) The effect of BX795 (2.5 μM), Dab (2.5 μM),
980 and their combination on cellular proliferation in 8505C and SW1736 cells after 48 h. (K–L)
981 Colony-formation assay in 8505C and SW1736 cells treated with BX795 (2.5 μM), Dab (2.5 μM),
982 or their combination. Quantification was performed using ImageJ. (M–N) Cellular migration as
983 measured with a wound-healing assay in 8505C and SW1736 cells treated with BX795 (2.5 μM),
984 Dab (2.5 μM), or their combination. Quantification was performed using the ImageJ software. (O–
985 P) Concentration-dependent effects of BX795 treatment on proliferation of patient-derived ATC
986 cells (ATC01 and ATC02). ATC01 was derived from a treatment-naïve patient tumor positive for
987 *BRAF* V600E mutation, and ATC02 was derived from a residual tumor in a patient with an
988 exceptional treatment response to Dab and trametinib, and the tumor was positive for *BRAF* V600E
989 mutation. (Q–R) The effects of treatment with BX795 (2.5 μM), Dab (2.5 μM), or their
990 combination on the proliferation of patient-derived ATC cells (ATC01 and ATC02). (S) The effect
991 of treatment with BX795 (2.5 μM), Dab (2.5 μM), or their combination on ATC spheroids in *BRAF*
992 V600E–mutant in the 8505C and SW1736 cell lines. (T) The effect of treatment with BX795 (2.5
993 μM), Dab (2.5 μM), or their combination on patient-derived ATC spheroids (ATC01 and ATC02).

994 All data are presented as the mean ± standard deviation. Statistical significance is indicated as ns
995 = nonsignificant; *p < 0.05; **p < 0.01; ***p < 0.001; ****p < 0.0001.
996
997 **Fig. 2: Effect of combination BX795 and dabrafenib (Dab) treatment in an orthotopic ATC**
998 ***in vivo* model.**

999 Mice were treated with BX795 (100 mg/kg), Dab (15 mg/kg), or their combination 5 days per
1000 week. After 2 weeks, tumors were excised and their volume (mm^3) (A) and weight (B) were
1001 measured. (C–D) *In vivo* tumor growth was analyzed by tumor luminescence analysis (photons/s)
1002 (C), and the fold change of each tumor was determined relative to the luminescence intensity of
1003 the tumor site at day 0 (D). Comparisons were made across treatment groups at days 0, 7, and 14.
1004 (E) Body weight of mice on day 14 of the study. All data are presented as mean ± standard error
1005 of the mean. Statistical significance is indicated as ns = nonsignificant; *p < 0.05; **p < 0.01;
1006 ***p < 0.001.
1007

1008 **Fig. 3: Combined PDPK1 and BRAF V600E inhibition induces apoptosis and DNA damage**
1009 **in *BRAF* V600E–mutant anaplastic thyroid cancer (ATC).**
1010 (A) Mutated *BRAF* V600E ATC cells (8505C) were treated for 48 h with BX795 (2.5 μM),
1011 dabrafenib (Dab) (2.5 μM), or their combination. Then, total and phosphorylated protein levels
1012 were measured using mass spectrometry. (A–C) The volcano plots show significantly upregulated
1013 proteins in red, significantly downregulated proteins in blue ($p < 0.05$), and non-significant
1014 proteins in gray. The x-axis represents $\log_2$ fold change, and the y-axis shows $-\log_{10}$(p-value). The
1015 dashed lines indicate thresholds for statistical significance and fold change. (D) The Venn
1016 diagrams shows shared and treatment-specific differentially expressed proteins and
1017 phosphorylated proteins across the treatment groups ($p < 0.05$). The overlapping regions represent
1018 a conserved core proteomic response, while the non-overlapping regions indicate pathway-specific
1019 effects of PDPK1 or BRAF inhibition. (E–G) Gene set enrichment analysis (GSEA) of ranked
1020 phosphorylated site changes following BX795 (E), Dab (F), or combination (G) treatment. The
1021 bar plots show normalized enrichment scores (NES) for Hallmark Kyoto Encyclopedia of Genes
1022 and Genomes (KEGG) signaling pathways. (H) Western blot analysis of the effect of BX795 (2.5
1023 μM), Dab (2.5 μM), or combination treatment on *BRAF* V600E–mutant ATC cell lines (8505C
1024 and SW1736) after 48 h. pMEK, total MEK, $pAKT^{308}$, total AKT, $pPDPK1^{S241}$, PARP-1, BCL2,

1025 and caspase-3 protein levels are shown, with β-actin used as a loading control. (I) Flow cytometry
1026 results of Annexin V/PI staining with BX795 (2.5 μM), Dab (2.5 μM), or combination treatment.
1027 (J) Western blot analysis of apoptosis regulatory proteins 40 h after treatment. $pBAD^{S112}$, BAD,
1028 BCL2, $pGSK3\beta^{Ser9}$, GSK3β, and the double-stranded DNA damage marker $pH2AX^{S139}$ are shown,
1029 with β-actin used as a loading control. Protein band density was measured and normalized to β-
1030 actin. The phosphorylated to total protein ratios were measured, and the values are listed above
1031 the phosphoprotein band. Protein band density of BCL-xL and $pH2AX^{S139}$ were also measured and
1032 normalized to β-actin. (K) Immunoprecipitation of BCL-xL and BCL2 with BAD 30 h after
1033 treatment with BX795 and Dab in *BRAF* V600E–mutant ATC cell lines. Protein band density was
1034 measured and normalized to the input protein band. The ratio of immunoprecipitated to total input
1035 protein was measured and is listed below the protein blot. P = phosphorylation. The superscript
1036 indicates the amino acid phosphorylation site. (L) The heatmap shows z-scored log_2-transformed
1037 abundance of apoptosis-related proteins for the BX795, Dab, and combination treatment groups in
1038 8505C ATC cells. The proteins are displayed in sequential order—BAD, TNFRSF10A, PARP1,
1039 FAS, BID, CASP3, CASP8, BAX, CASP9, CASP7, BCL2L1, and BAK1—with hierarchical
1040 clustering applied to the rows. (M) The effect of BX795 (2.5 μM), Dab (2.5 μM), or combination
1041 treatment for 16 h on γH2AX foci formation in the 8505C and SW1736 ATC cell lines using
1042 immunofluorescence. γH2AX was labelled with Alexa Fluor™ 546 secondary antibody, with
1043 DAPI used for nuclear staining. A Zeiss LSM 800 confocal microscope was used to examine the
1044 cells (400× magnification). The number of foci per cell was quantified using ImageJ. All data are
1045 presented as the mean ± standard error of the mean of 25 cells. Statistical significance is indicated
1046 as ns = nonsignificant; *$p < 0.05$; **$p < 0.01$; ***$p<0.001$; ****$p < 0.0001$. (N) Western blot
1047 analysis of the effect of BX795 (2.5 μM), Dab (2.5 μM), or combination treatment for 16 h on
1048 DNA damage–dependent proteins (pATM, total ATM, pCHK2, Total CHK2, and pCHK1). β-
1049 Actin was used as a loading control. (O) Cell cycle analysis after BX795 (2.5 μM), Dab (2.5 μM),
1050 or combination treatment for 16 h in *BRAF* V600E–mutant ATC cell lines (8505C and SW1736).
1051 Cells were stained with propidium iodide (PI) and analyzed by fluorescence-activated cell sorting.
1052 The DNA content was measured, 2N (diploid) and 4N (tetraploid), based on the PI-stained DNA
1053 content. (P) The effect of BX795 (2.5 μM), Dab (2.5 μM), or combination treatment for 16 h on
1054 DNA repair proteins—cyclin D, cyclin B, pcdc25c, pCDK1, total CDK1, pH3A, H3A, and cyclin
1055 A2—by immunoblotting. β-actin was used as a loading control. The ratio of phospho-H3A to total
1056 H3A was measured and is listed below the phospho-H3A protein band. All data are presented as

1057 the mean ± standard deviation. Statistical significance is indicated as ns = nonsignificant; *p <
1058 0.05; **p < 0.01; ***p < 0.001; ****p < 0.0001. (Q) Analysis of the effect of combination BX795
1059 (2.5 μM) and Dab (2.5 μM) treatment for 16 h followed by proteasomal degradation inhibition for
1060 6 h (MG132, 10 μM). Protein band density was measured and normalized to β-actin. (R) The
1061 heatmap shows z-scored log2-transformed phosphorylation levels of DNA damage response, DNA
1062 repair, and cell-cycle regulatory proteins for the BX795, Dab, and combination treatment groups
1063 in 8505C ATC cell line. Proteins are displayed in sequential order as RAD50, CDK1, MCM2,
1064 PRKDC, RB1, TP53BP1, TP53, XRCC1, XRCC5, LIG1, MDC1, and MSH6, with supervised
1065 hierarchical clustering applied to the rows. The color scale represents relative protein levels (red
1066 = higher; blue = lower).
1067
1068 **Fig. 4: The effects of BX795 and dabrafenib (Dab) treatment on reactive oxygen species**
1069 **(ROS), mitochondrial function, and bioenergetics in *BRAF* V600E–mutant anaplastic**
1070 **thyroid cancer (ATC) cell lines.**
1071 Mutated BRAF V600E cell were treated with BX795 (2.5 μM), Dab (2.5 μM), or their
1072 combination. (A) Total cellular ROS was measured using the DCFH-DA fluorescent dye and
1073 quantified with flow cytometry. (B) Mitochondrial superoxide was measured based on MitoSOX
1074 red fluorescence, quantified with flow cytometry. (C–D) The mitochondrial content was assessed
1075 by MitoTracker green fluorescence, as quantified by flow cytometry and visualized with live-cell
1076 confocal microscopy (Zeiss LSM 800, 400× magnification). (E) The mitochondrial membrane
1077 potential was evaluated by TMRM (100 nM) fluorescence and analyzed by flow cytometry. (F)
1078 The oxygen consumption rate (OCR) was measured using a Seahorse analyzer with sequential
1079 injections of oligomycin (Oligo), 2,4-dinitrophenol (DNP), and antimycin A plus rotenone
1080 (Rot+AA). The data were normalized to the total protein content, and maximal respiration and
1081 adenosine triphosphate (ATP)-linked respiration were quantified accordingly. (G) The heatmap
1082 shows z-scored $\log_2$-transformed abundance of proteins associated with mitochondrial oxidative
1083 phosphorylation, the tricarboxylic acid (TCA) cycle, mitochondrial ribosomal, transport, and
1084 mitochondrial dynamics–associated proteins in 8505C ATC cells treated with BX795 (2.5 μM),
1085 Dab (2.5 μM), or their combination. The proteins include representatives of electron transport
1086 chain complexes I–V (NDUF subunits, SDHA–D, UQCRC1/2, COX subunits, and ATP5
1087 subunits), TCA cycle enzymes (IDH1, IDH2, IDH3, FH, OGDH, DLST, CS, MDH2, and
1088 PDHA1/PDHB), mitochondrial transport and structure (TOMM20, TIMM23, VDAC1–3, MFN1,

1089 OPA1, DNM1L), and mitochondrial genome maintenance (TFAM). Hierarchical clustering was
1090 applied to the rows. The color scale represents relative protein abundance (red = higher; blue =
1091 lower). All data are expressed as the mean ± standard deviation. Statistical significance is indicated
1092 as ns = nonsignificant; *p < 0.05; **p < 0.01; ***p < 0.001; ****p < 0.0001.
1093
1094 **Fig. 5: Reactive oxygen species (ROS) scavenging attenuates combination BX795 and**
1095 **dabrafenib (Dab) treatment effect while CHK2 inhibition leads to mitotic slippage and**
1096 **partial apoptotic reversal.**
1097 (A) Time-dependent effect of combination BX795 and Dab treatment based on propidium iodide
1098 (PI) staining, showing the proportion of cells arrested in the G2/M phase. Cells were stained with
1099 PI and analyzed by fluorescence-activated cell sorting. The results are presented as the mean ±
1100 standard deviation. Statistical significance is indicated as ns = nonsignificant; *p < 0.05; **p <
1101 0.01; ***p < 0.001; ****p < 0.0001. (B) Intracellular ROS levels were measured using DCFH-
1102 DA staining and analyzed by flow cytometry. The results are presented as the mean ± standard
1103 deviation. (C–E) The effects of *N*-acetyl cysteine (NAC) (5 mM) on combination treatment–
1104 induced responses in *BRAF* V600E–mutant ATC cell lines. (C) ROS generation was analyzed by
1105 DCFH-DA staining and is presented as the mean ± standard deviation. (D) Apoptosis was assessed
1106 based on Annexin V/PI staining. (E) Immunoblot analysis of PARP-1 cleavage using β-actin as a
1107 loading control. The densitometric quantification of cleaved vs pro-PARP cleavage in relation to
1108 loading control is shown below the bands. (F) The effect of the mitochondrial ROS scavenger
1109 MitoQ on combination treatment–induced G2/M arrest in *BRAF* V600E–mutant ATC cell lines.
1110 The DNA content was measured, 2N (diploid) and 4N (tetraploid), based on PI staining. The results
1111 are presented as the mean ± standard deviation. Statistical significance is indicated as ns =
1112 nonsignificant; *p < 0.05; **p < 0.01; ***p < 0.001; ****p < 0.0001. (G–H) The impact of CHK2
1113 phosphorylation inhibitor BML-277 (ML277) on combination BX795 and Dab treatment-induced.
1114 (G) Cell cycle arrest was analyzed by PI staining and flow cytometry. (H) Antiproliferative effect
1115 in *BRAF* V600E–mutant ATC cells. The DNA content was measured, 2N (diploid) and 4N
1116 (tetraploid), based on PI staining. The results are presented as the mean ± standard deviation.
1117 Statistical significance is indicated as ns = nonsignificant; *P < 0.05; **P < 0.01; ***P < 0.001;
1118 ****P < 0.0001. (I) Apoptosis was measured with Annexin V/PI staining and flow cytometry. The
1119 results are presented as mean ± standard deviation. Statistical significance is indicated as ns =
1120 nonsignificant; *p < 0.05; **p < 0.01; ***p < 0.001; ****p < 0.0001.

1121
1122 **Supplemental Figures**

1123 **Fig. S1: PDPK1 expression, the efficacy of PDPK1 inhibitors, and the effect of combination**
1124 **PDPK1 and BRAF V600E inhibition in anaplastic thyroid cancer (ATC) cells.**

1125 (A) The box-and-whisker plot shows the Chronos gene effect scores for PDPK1 across the top 10
1126 cancer lineages from the DepMap 25Q3 dataset. The scores represent the impact of PDPK1
1127 knockout on cell fitness, where more negative values indicate greater essentiality. Individual dots
1128 represent cell lines within each lineage, and boxes denote the median and interquartile range. The
1129 thyroid cancer lineage is highlighted in red. (B) PDPK1 messenger RNA (mRNA) expression
1130 presented as Expression $\log_2$(TPM+1) among different thyroid cancer cell lines: ATC, follicular
1131 thyroid cancer (FTC), well-differentiated thyroid cancer (WDTC), medullary thyroid cancer
1132 (MTC), and poorly differentiated thyroid cancer (PDTC). (C) The box-and-whicker plot shows the
1133 Chronos gene effect scores for PDPK1 across thyroid cancer subtypes from the DepMap 25Q3
1134 dataset. Individual data points represent cell lines, and boxes denote the median and interquartile
1135 range. ATC is highlighted in red. (D) Data from quantitative high-throughput drug screening in
1136 ATC cell lines (8505C, THJ16T, and THJ11T). Comparison of half-maximal inhibitory
1137 concentration (IC_{50}) < 10 μM and drug-response curve class of < 2.2 for known PDPK1 inhibitors
1138 (BX795, GSK2334470, OSU-03012, DTXSID90678515, and BX912) after treatment for 48 h. (E)
1139 PRISM drug sensitivity scores for BX795 (24Q2) across thyroid cancer subtypes, including
1140 WDTC, ATC, PDTC, and MTC. More negative values indicate greater sensitivity to BX795. The
1141 data are derived from pooled cell line responses within each subtype. (F) To analyze the effect of
1142 BX795 treatment, *BRAF* V600E–mutant ATC cell lines (8505C and SW1736) were treated with
1143 BX795 (2.5 or 5 μM) for 48 h, and then the levels of non-phosphorylated and phosphorylated
1144 mTOR, AKT (T^{308}), H_2AX (S^{15}), and S6K were evaluated by immunoblotting using β-actin as a

1145 loading control. (G) *BRAF* V600E–mutant ATC cell lines (8505C and SW1736) were transiently
1146 silenced with Control siRNA, PDPK1si1, or PDPK1si2 in combination with BX795 (2.5 μM) for
1147 48 h, and then the levels of phosphorylated PDPK1 (S^{245}), H_2AX, and PDPK1 were evaluated by
1148 immunoblotting using β-actin as a loading control. Their effect on cell proliferation was also
1149 measured. The results are presented as the mean ± SD. Statistical significance is indicated as ns =
1150 nonsignificant; *$p < 0.05$; **$p < 0.01$; ***$p < 0.001$; ****$p < 0.0001$. (H–I) Representative images
1151 of the colony-formation assay (H) and cellular migration (I) with BX795 and dabrafenib (Dab)
1152 treatment alone and their combination in *BRAF* V600E–mutant ATC cells. The representative
1153 images correspond to the data shown in Fig. 1K–N.
1154
1155 **Fig. S2: Combination BX795 and dabrafenib (Dab) treatment *in vivo*.**
1156 (A–B) Representative tumor images from all mouse groups at the end of the study by sex. (C–D)
1157 Analysis of the tumor weight (C) and tumor volume (D) at the study endpoint by sex. The results
1158 are presented as the mean ± standard error of the mean. Statistical significance is indicated as ns =
1159 nonsignificant; *$p < 0.05$.
1160
1161 **Fig. S3: Combination BX795 and dabrafenib (Dab) treatment induces apoptosis and G2**
1162 **arrest.**
1163 (A) The effect of treatment with BX795 (2.5 μM), Dab (2.5 μM), or their combination for 40 h
1164 on BCL2 and phospho-PDPK1 (pPDPK1) protein levels in *BRAF* V600E–mutant ATC cells
1165 (8505C). Immunofluorescence was performed with BCL2 labeled using Alexa Fluor™ 633
1166 secondary antibody and pPDPK1 labeled with Alexa Fluor™ 546 secondary antibody; DAPI was
1167 used as a nuclear counterstain. Images were acquired using a Zeiss LSM 800 confocal microscope

1168 at 400× magnification. (B) Densitometry results for the proteins shown in Fig. 4P, normalized to
1169 β-actin. The y-axis is the fold change relative to the control.
1170
1171 **Fig. S4: The effect of combination BX795 and dabrafenib (Dab) treatment on basal**
1172 **respiration, the mitochondrial membrane potential, DNA damage proteins, and cell cycle**
1173 **arrest.**
1174 (A) Analysis of the effect of treatment with BX795, Dab, or their combination on basal respiration
1175 in *BRAF* V600E–mutant ATC cell lines (8505C and SW1736), measured with the Seahorse assay.
1176 The basal respiration rate was normalized to the total protein content and is presented as the mean
1177 ± standard deviation. (B) Mitochondrial integrity was assessed by JC-1 staining after combination
1178 treatment, with the red-to-green fluorescence ratio determined with flow cytometry. The results
1179 are presented as mean ± standard deviation. (C) Immunoblot analysis of oxidative phosphorylation
1180 proteins following treatments, using β-actin as a loading control. Protein band density was
1181 determined and normalized to β-actin. The y-axis is the fold change relative to the control
1182 (DMSO). (D–E) Time-dependent effects (0–40 h) of treatment with BX795 (2.5 μM), Dab (2.5
1183 μM), or their combination on the mitochondrial membrane potential (D) and mitochondrial content
1184 (E) in *BRAF* V600E–mutant ATC cell lines. The mitochondrial membrane potential was assessed
1185 using TMRM (100 nM) fluorescence, and the mitochondrial content was measured with
1186 MitoTracker Green dye, with flow cytometry used for quantification. The data are presented as the
1187 mean ± standard deviation. (F) Immunoblot analysis of phosphorylated CHK2 (pCHK2),
1188 phosphorylated ATM (pATM), and phosphorylated H2AX (pH2AX) levels in *BRAF* V600E–
1189 mutant ATC cell lines treated with BX795 (2.5 μM) and Dab (2.5 μM) in the presence or absence
1190 of *N*-acetyl cysteine (NAC) (5 mM). β-Actin was used as a loading control. (G) Representative
1191 results of Fig. 5G. (H–I) Analysis of the effect of the AZD7762 on cell cycle arrest and the

1192 antiproliferative effect induced by combination BX795 and Dab treatment in *BRAF* V600E–
1193 mutant ATC cells (SW1736). The results are presented as the mean ± standard deviation. Statistical
1194 significance is indicated as ns = nonsignificant; *$p < 0.05$; **$p < 0.01$; ***$p < 0.001$; ****$p <$
1195 0.0001.

1196
1197
1198
1199
1200
1201
1202
1203
1204
1205
1206
1207
1208
1209
1210
1211
1212
1213
1214
1215
1216
1217
1218
1219

Fig. 1a

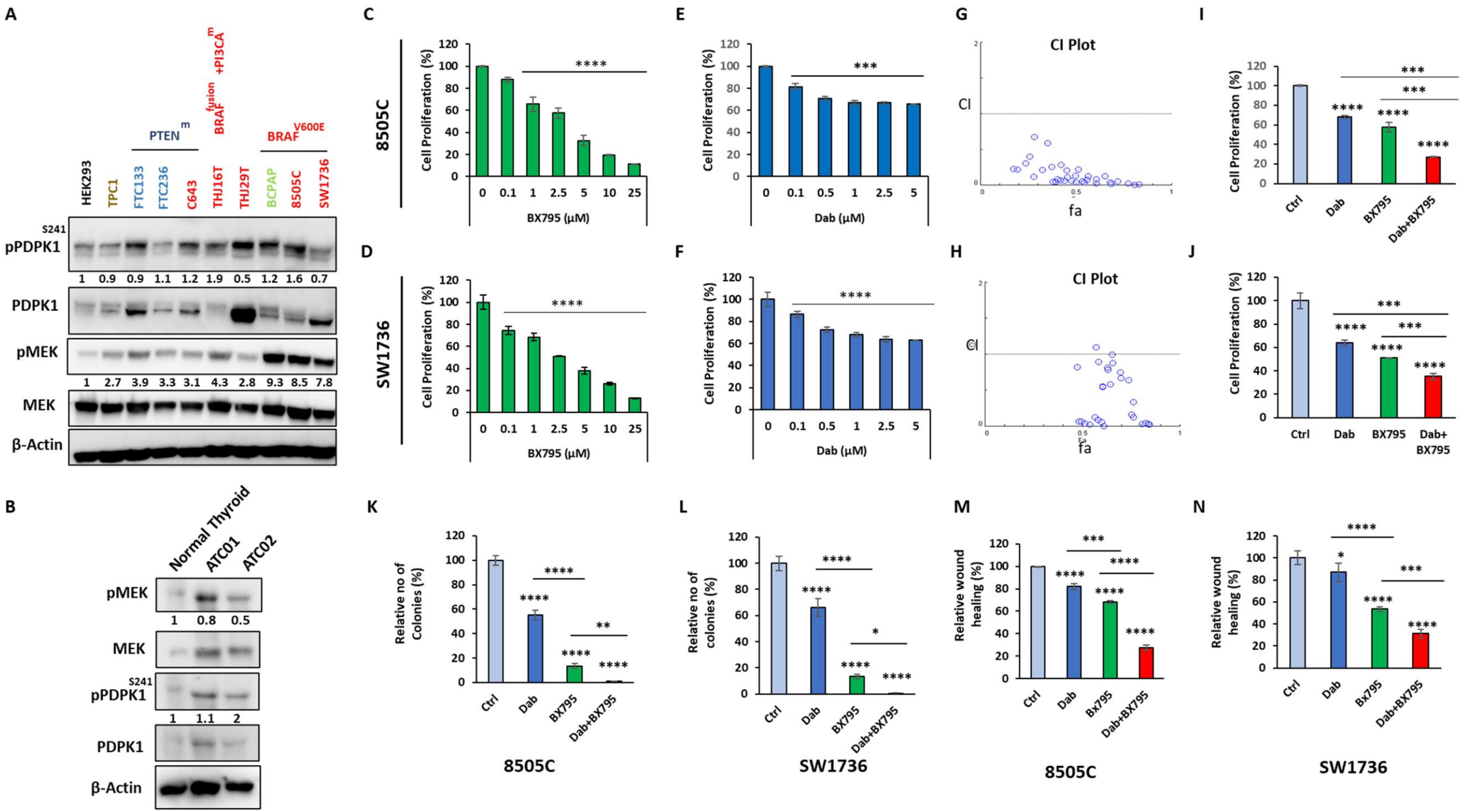
A
HEK293
TPC1
FTC133
FTC236
C643
THJ16T
THJ29T
BCPAP
8505C
SW1736
PTEN m
BRAF fusion +PI3CA m
BRAF V600E
S241
pPDPK1
1 0.9 0.9 1.1 1.2 1.9 0.5 1.2 1.6 0.7
PDPK1
pMEK
1 2.7 3.9 3.3 3.1 4.3 2.8 9.3 8.5 7.8
MEK
β-Actin
B
Normal Thyroid
ATC01
ATC02
pMEK
1 0.8 0.5
MEK
S241
pPDPK1
1 1.1 2
PDPK1
β-Actin
C
8505C
Cell Proliferation (%)
BX795 (μM)
D
SW1736
E
Dab (μM)
F
G
CI Plot
CI
fa
H
I
Ctrl
Dab
BX795
Dab+BX795
J
Dab+ BX795
K
Relative no of Colonies (%)
L
Relative no of colonies (%)
M
Relative wound healing (%)
N

Fig. 1b

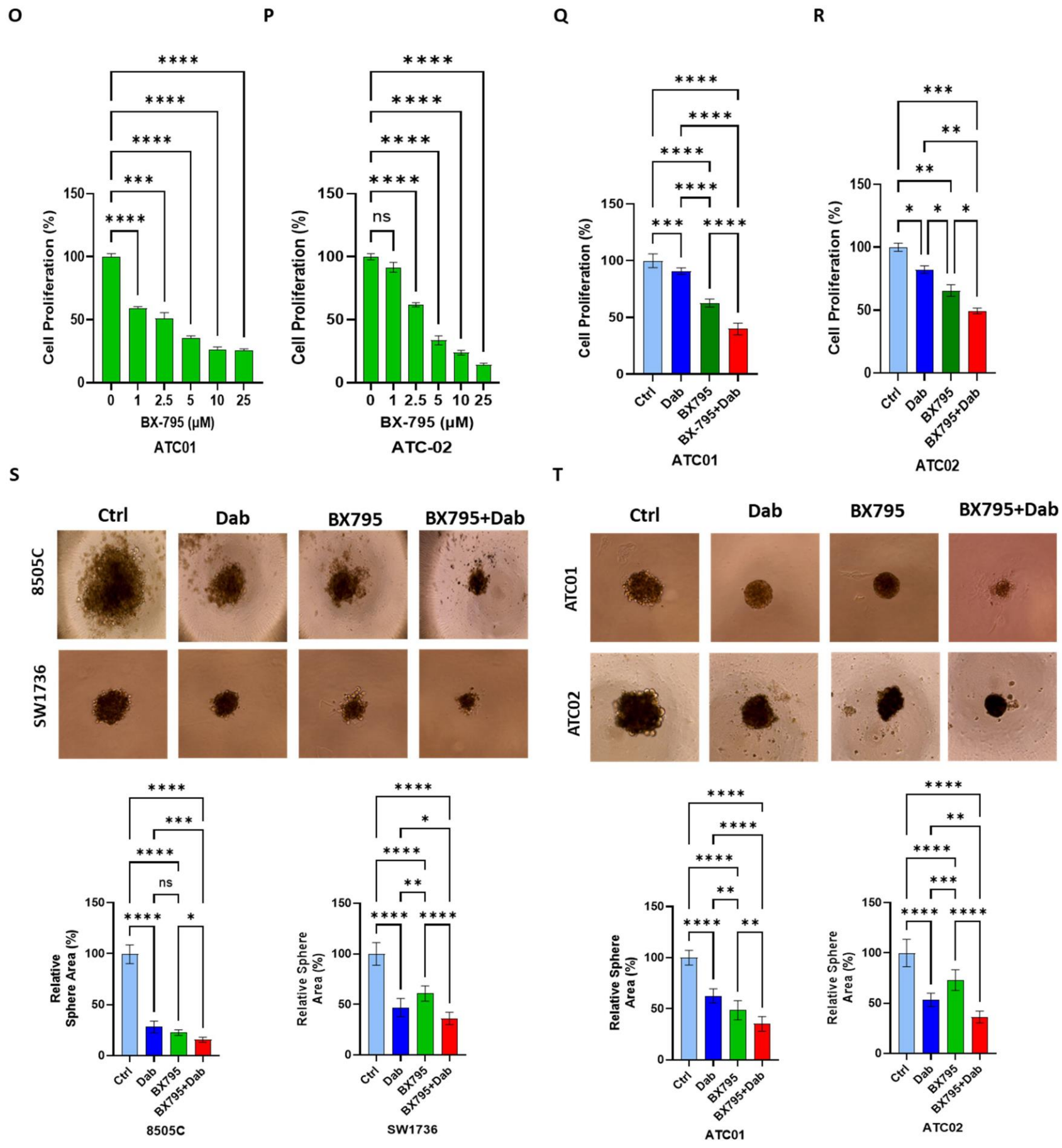
O
P
Q
R
Cell Proliferation (%)
BX-795 (μM)
ATC01
ATC-02
Ctrl
Dab
BX795
BX-795+Dab
BX795+Dab
ATC02
S
T
8505C
SW1736
Relative Sphere Area (%)

Fig. 2

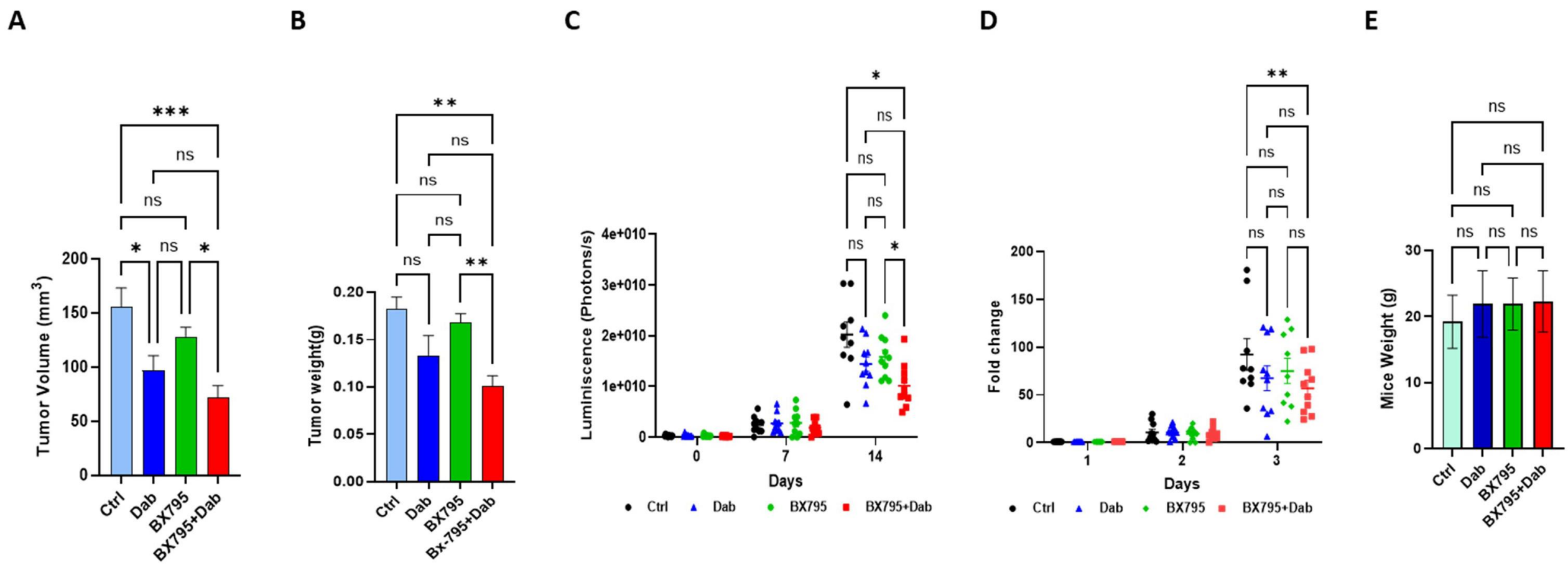
A
B
C
D
E
Tumor Volume (mm3)
Tumor weight(g)
Luminiscence (Photons/s)
Fold change
Mice Weight (g)
Days
Ctrl
Dab
BX795
BX795+Dab
Bx-795+Dab
ns
*
**
***

Fig. 3a

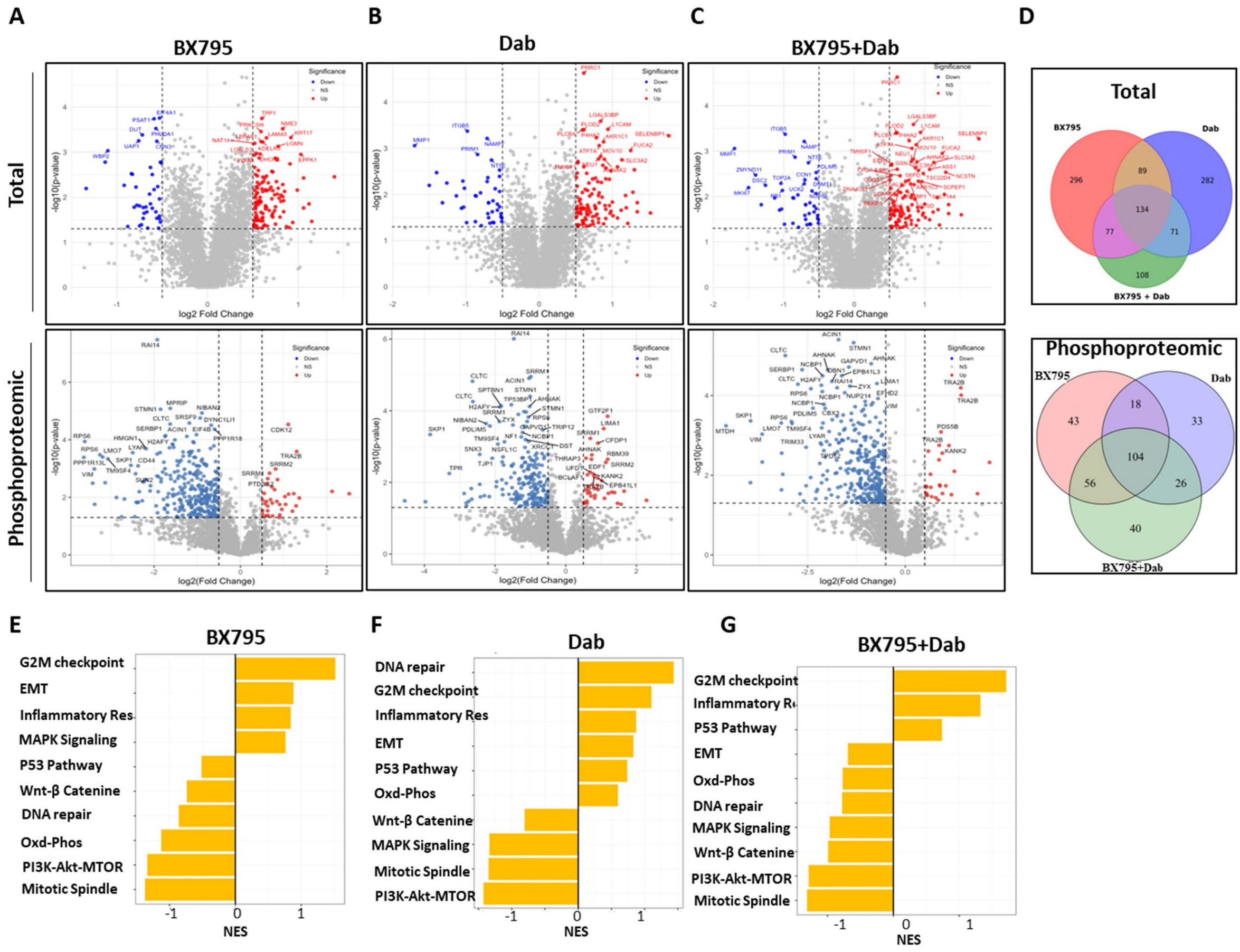
A
B
C
D
BX795
Dab
BX795+Dab
Total
Phosphoproteomic
Significance
Down
NS
Up
-log10(p-value)
log2 Fold Change
log2(Fold Change)
Total
BX795
Dab
BX795 + Dab
296
89
282
134
77
71
108
Phosphoproteomic
BX795
Dab
BX795+Dab
43
18
33
104
56
26
40
E
F
G
BX795
Dab
BX795+Dab
G2M checkpoint
EMT
Inflammatory Res
MAPK Signaling
P53 Pathway
Wnt-β Catenine
DNA repair
Oxd-Phos
PI3K-Akt-MTOR
Mitotic Spindle
NES

Fig. 3b

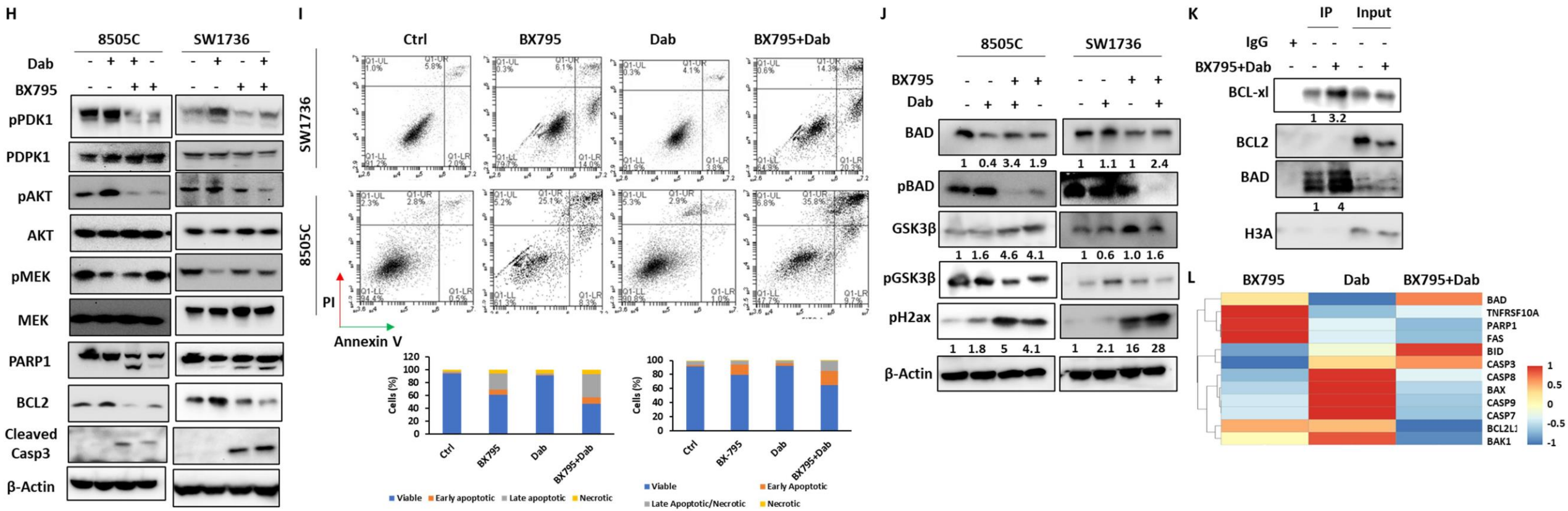
H
8505C
SW1736
Dab
BX795
pPDK1
PDPK1
pAKT
AKT
pMEK
MEK
PARP1
BCL2
Cleaved Casp3
β-Actin
I
Ctrl
BX795
Dab
BX795+Dab
SW1736
8505C
PI
Annexin V
Cells (%)
Viable
Early apoptotic
Late apoptotic
Necrotic
Early Apoptotic
Late Apoptotic/Necrotic
J
BAD
pBAD
GSK3β
pGSK3β
pH2ax
β-Actin
K
IP
Input
IgG
BCL-xl
BCL2
BAD
H3A
L
BAD
TNFRSF10A
PARP1
FAS
BID
CASP3
CASP8
BAX
CASP9
CASP7
BCL2L1
BAK1

Fig. 3c

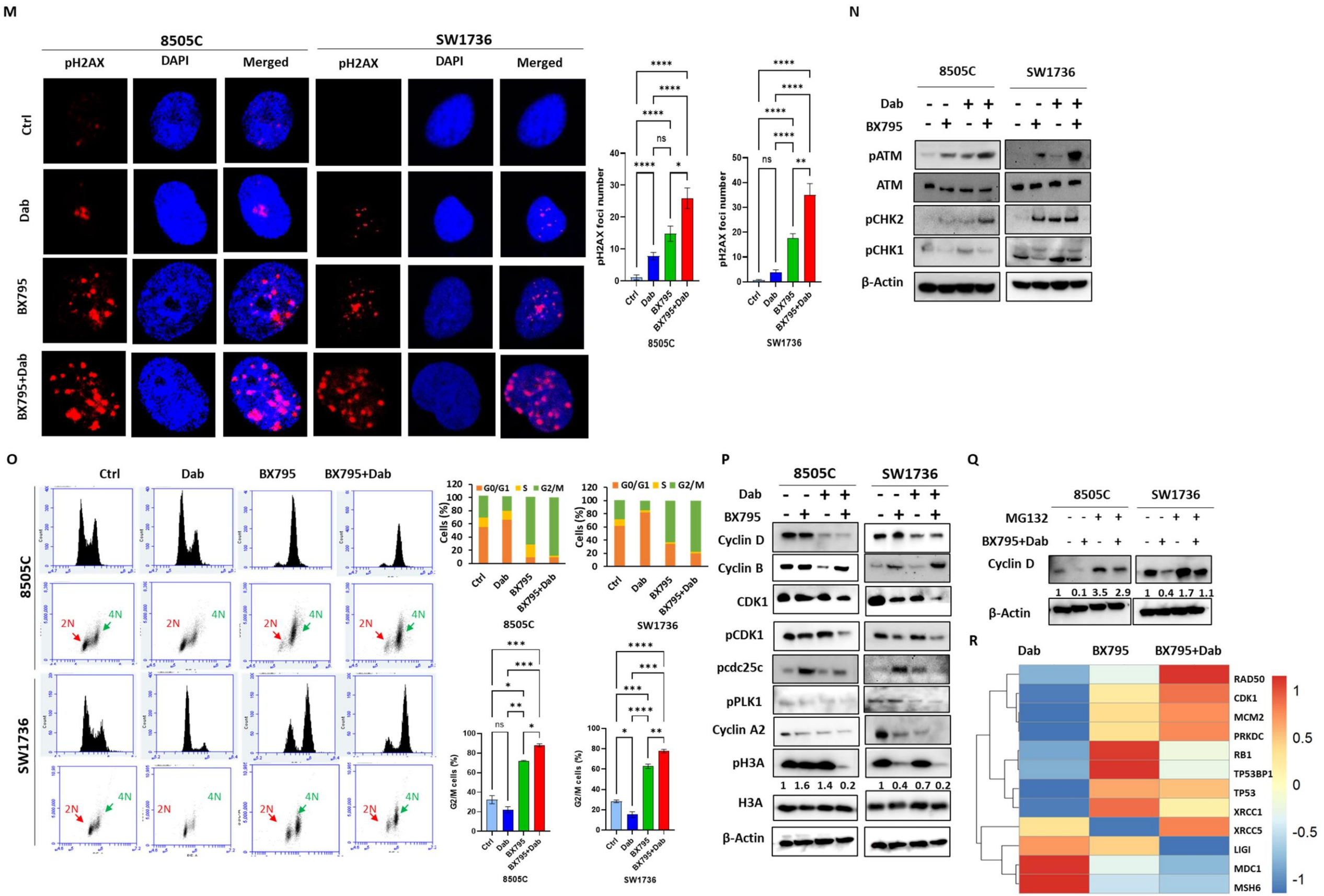
M
8505C
SW1736
pH2AX
DAPI
Merged
Ctrl
Dab
BX795
BX795+Dab
pH2AX foci number
Ctrl
Dab
BX795
BX795+Dab
8505C
SW1736
N
8505C
SW1736
Dab
BX795
pATM
ATM
pCHK2
pCHK1
β-Actin
O
Ctrl
Dab
BX795
BX795+Dab
8505C
SW1736
2N
4N
G0/G1
S
G2/M
Cells (%)
G2/M cells (%)
P
8505C
SW1736
Dab
BX795
Cyclin D
Cyclin B
CDK1
pCDK1
pcdc25c
pPLK1
Cyclin A2
pH3A
1 1.6 1.4 0.2
1 0.4 0.7 0.2
H3A
β-Actin
Q
8505C
SW1736
MG132
BX795+Dab
Cyclin D
1 0.1 3.5 2.9
1 0.4 1.7 1.1
β-Actin
R
Dab
BX795
BX795+Dab
RAD50
CDK1
MCM2
PRKDC
RB1
TP53BP1
TP53
XRCC1
XRCC5
LIGI
MDC1
MSH6
1
0.5
0
-0.5
-1

Fig. 4

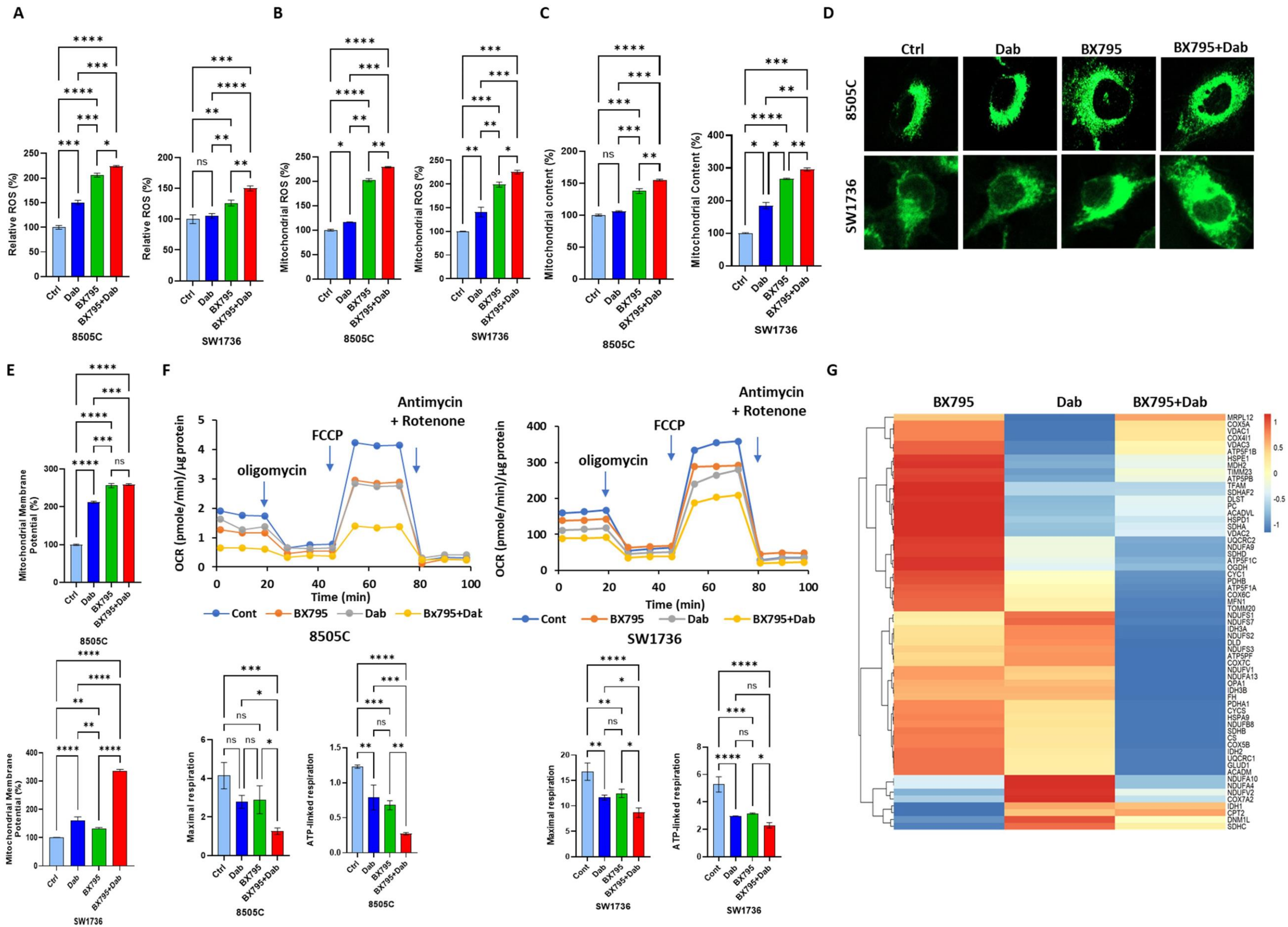
A
Relative ROS (%)
Ctrl
Dab
BX795
BX795+Dab
8505C
SW1736
B
Mitochondrial ROS (%)
C
Mitochondrial content (%)
Mitochondrial Content (%)
D
Ctrl
Dab
BX795
BX795+Dab
8505C
SW1736
E
Mitochondrial Membrane Potential (%)
F
Antimycin + Rotenone
FCCP
oligomycin
OCR (pmole/min)/µg protein
Time (min)
Cont
BX795
Dab
Bx795+Dab
BX795+Dab
Maximal respiration
ATP-linked respiration
G
BX795
Dab
BX795+Dab
MRPL12
COX5A
VDAC1
COX4I1
VDAC3
ATP5F1B
HSPE1
MDH2
TIMM23
ATP5PB
TFAM
SDHAF2
DLST
PC
ACADVL
HSPD1
SDHA
VDAC2
UQCRC2
NDUFA9
SDHD
ATP5F1C
OGDH
CYC1
PDHB
ATP5F1A
COX6C
MFN1
TOMM20
NDUFS1
NDUFS7
IDH3A
NDUFS2
DLD
NDUFS3
ATP5PF
COX7C
NDUFV1
NDUFA13
OPA1
IDH3B
FH
PDHA1
CYCS
HSPA9
NDUFB8
SDHB
CS
COX5B
IDH2
UQCRC1
GLUD1
ACADM
NDUFA10
NDUFA4
NDUFV2
COX7A2
IDH1
CPT2
DNM1L
SDHC

Fig. 5a

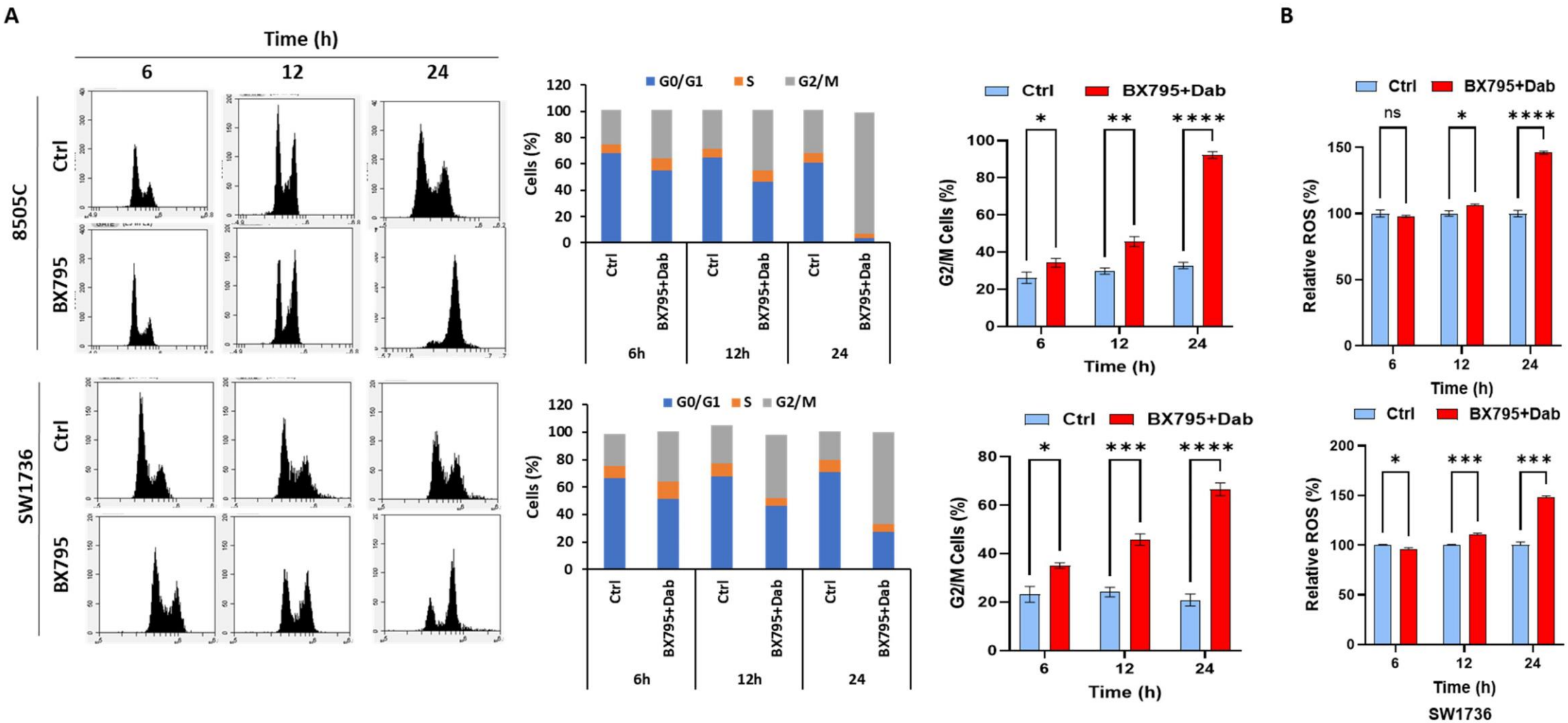
A
Time (h)
6
12
24
8505C
Ctrl
BX795
SW1736
Ctrl
BX795
G0/G1
S
G2/M
Cells (%)
Ctrl
BX795+Dab
6h
12h
24
G2/M Cells (%)
Time (h)
B
Relative ROS (%)
ns
SW1736

Fig. 5b

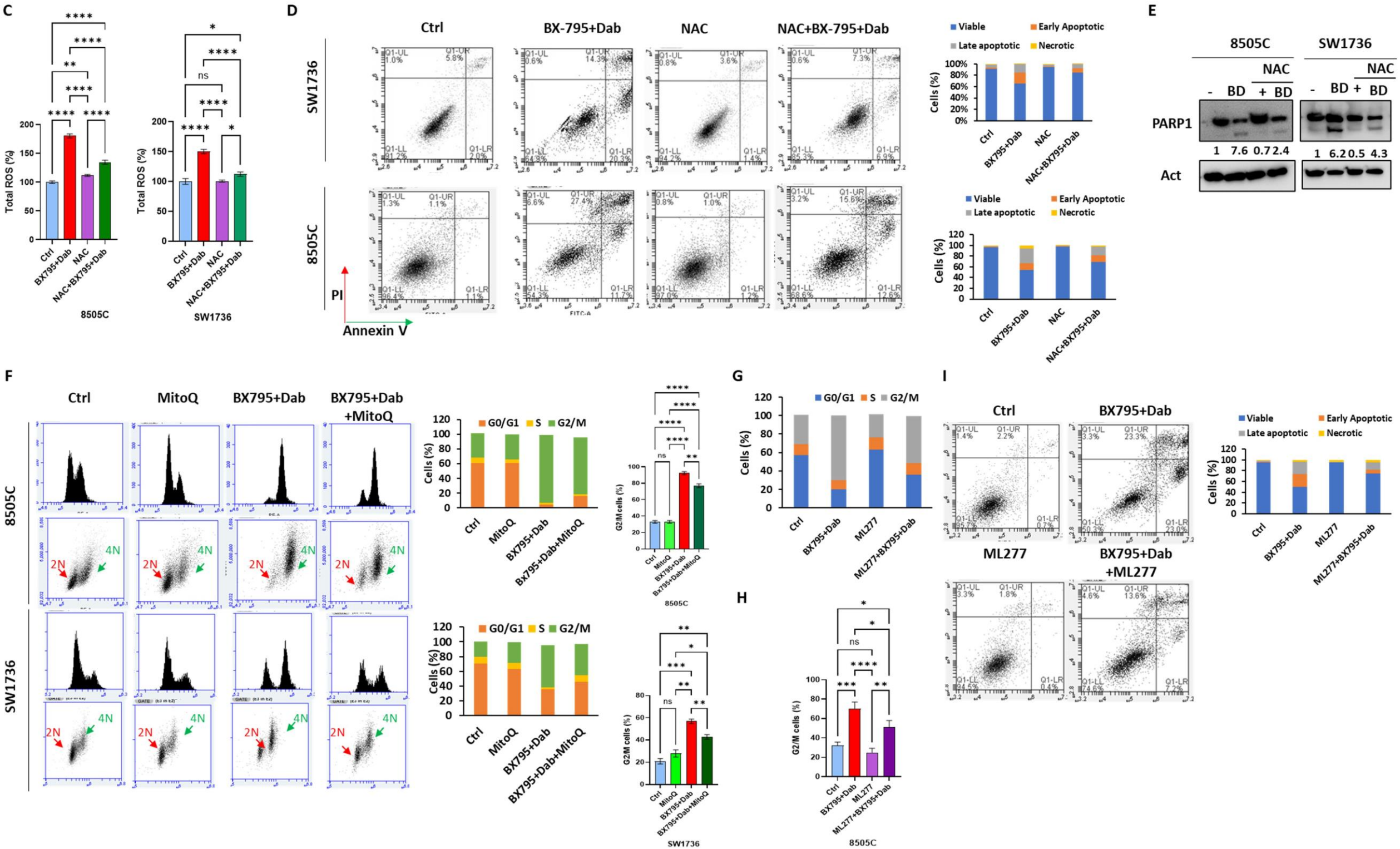
C
Total ROS (%)
Ctrl
BX795+Dab
NAC
NAC+BX795+Dab
8505C
SW1736
D
Ctrl
BX-795+Dab
NAC
NAC+BX-795+Dab
SW1736
8505C
PI
Annexin V
Viable
Early Apoptotic
Late apoptotic
Necrotic
Cells (%)
E
8505C
SW1736
NAC
BD
PARP1
Act
F
Ctrl
MitoQ
BX795+Dab
BX795+Dab +MitoQ
8505C
SW1736
2N
4N
G0/G1
S
G2/M
Cells (%)
G2/M cells (%)
G
ML277
ML277+BX795+Dab
H
I
BX795+Dab +ML277